



Research Article

Unusual He-ion irradiation strengthening and inverse layer thickness-dependent strain rate sensitivity in transformable high-entropy alloy/metal nanolaminates: A comparison of $\text{Fe}_{50}\text{Mn}_{30}\text{Co}_{10}\text{Cr}_{10}/\text{Cu}$ vs $\text{Fe}_{50}\text{Mn}_{30}\text{Co}_{10}\text{Ni}_{10}/\text{Cu}$

Y.F. Zhao¹, H.H. Chen¹, D.D. Zhang, J.Y. Zhang*, Y.Q. Wang, K. Wu, G. Liu*, J. Sun

State Key Laboratory for Mechanical Behavior of Materials, Xi'an Jiaotong University, Xi'an 710049, China

ARTICLE INFO

Article history:

Received 2 July 2021

Revised 25 September 2021

Accepted 7 October 2021

Available online 29 January 2022

Keywords:

High entropy alloy/metal nanolaminates

Interfaces

Irradiation hardening

Strain rate sensitivity

Size effects

ABSTRACT

In this work, we prepare transformable HEA/Cu nanolaminates (NLs) with equal individual layer thickness (h) by the magnetron sputtering technique, i.e., $\text{Fe}_{50}\text{Mn}_{30}\text{Co}_{10}\text{Cr}_{10}/\text{Cu}$ and $\text{Fe}_{50}\text{Mn}_{30}\text{Co}_{10}\text{Ni}_{10}/\text{Cu}$, and comparatively study He-ion irradiation effects on their microstructure and mechanical properties. It appears that the as-deposited HEA/Cu NLs manifest two size h -dependent hardness regimes (i.e., increased hardness at small h and hardness plateau at large h), while the He-implanted ones exhibit monotonically increased hardness. Contrary to the fashion that smaller h renders less irradiation hardening in bimetal NLs, the $\text{Fe}_{50}\text{Mn}_{30}\text{Co}_{10}\text{Cr}_{10}/\text{Cu}$ NLs manifest the trend that smaller h leads to greater irradiation hardening. By contrast, the $\text{Fe}_{50}\text{Mn}_{30}\text{Co}_{10}\text{Ni}_{10}/\text{Cu}$ NLs exhibit the maximum irradiation hardening at a critical $h = 50$ nm. Below this critical size, smaller h results in lower radiation hardening (similar to bimetal NLs), while above this size, smaller h results in greater radiation hardening (similar to $\text{Fe}_{50}\text{Mn}_{30}\text{Co}_{10}\text{Cr}_{10}/\text{Cu}$ NLs). Moreover, these transformable HEA/Cu NLs display inverse h -dependent strain rate sensitivity (SRS m) before and after He-ion irradiation. Nevertheless, compared with as-deposited samples, the irradiated $\text{Fe}_{50}\text{Mn}_{30}\text{Co}_{10}\text{Cr}_{10}/\text{Cu}$ NLs display reduced SRS, while the irradiated $\text{Fe}_{50}\text{Mn}_{30}\text{Co}_{10}\text{Ni}_{10}/\text{Cu}$ NLs display enhanced SRS. Such unusual size-dependent irradiation strengthening and inverse h effect on SRS in irradiated samples were rationalized by considering the blocking effects of He bubbles on dislocation nucleation and motion, i.e., dislocations shearing or bypassing He bubbles.

© 2022 Published by Elsevier Ltd on behalf of The editorial office of Journal of Materials Science & Technology.

1. Introduction

It is a great challenge for the development of advanced nuclear fission reactors at present to design damage-resistant structural materials. Apart from high temperature and high pressure, these structural materials also undertake high levels of irradiation [1,2]. Irradiation introduces point defects, vacancies and interstitial atoms (Frenkel pairs), which can evolve into larger clusters of point defects, thereby degrading the mechanical properties of structural materials [3]. The design of irradiation resistant materials needs to reduce the defect concentration mainly by either increasing the combination rate of irradiation defects or increasing material defect sinks, such as grain boundaries (GBs) and heterogeneous in-

terfaces, to trap more irradiation defects for their annihilation, or both [4].

Unlike traditional dilute alloys, for high-entropy alloys (HEAs), their composition complexity and severe lattice distortion can effectively change the defect migration behavior and enhance the combination rate of irradiation defects [5]. Previous work demonstrated that the defect migration behavior in HEAs altered from the long-distance 1D mode (in binary alloys) to the short-distance 3D mode, which significantly improved the vacancy-interstitial recombination rate, and thus enabled them to become good candidates for irradiation-resistant materials [5,6]. Furthermore, Zhang et al. [7] conducted in-depth simulations on the electronic structure and material properties of HEAs and revealed that the electron and phonon mean free paths can be reduced by the chemical disorder of HEAs, which subsequently can suppress the evolution and growth of irradiation-induced defects, leading to great irradiation resistance. In general, due to their unique and intrinsic characters, such as sluggish diffusion effects and severe lattice dis-

* Corresponding authors.

E-mail addresses: jinyuzhang1002@mail.xjtu.edu.cn (J.Y. Zhang), lgsammer@mail.xjtu.edu.cn (G. Liu).

¹ Equal Contributors.

tortion effects, HEAs generally possess outstanding irradiation tolerance [5,8,9], high strength and ductility [10–12], excellent thermal stability [13,14] and great fatigue resistance [15–17]. It is well recognized that the HEAs, which break the traditional alloy design principles, open up a new territory for exploring outstanding damage-resistant materials [18–20].

A previous work [21] proved that the dual-phase HEAs manifested better mechanical properties than traditional alloy systems, owing to their strain-induced transformation from the FCC to HCP phase and the dynamic-strain partitioning behavior. As increasing the HCP-phase fraction, both strength and ductility of the dual-phase HEAs increase at higher local strains [22]. More specific, a transformation-induced plasticitydual-phase HEA (TRIP-DP-HEA), i.e., the $\text{Fe}_{50}\text{Mn}_{30}\text{Co}_{10}\text{Cr}_{10}$ HEA, was designed by decreasing phase stability to combine interface hardening (resulting from reduced thermal stability of the high-temperature phase) and transformation-induced hardening (resulting from the reduced mechanical stability of the room-temperature phase) to overcome the strength-ductility trade-off [21]. This $\text{Fe}_{50}\text{Mn}_{30}\text{Co}_{10}\text{Cr}_{10}$ HEA with the initial FCC and HCP dual-phase structure behaves higher strength and ductility, due to the increased strain hardening ability caused by the mechanically stress-driven FCC to HCP transformation [23,24]. It is thus anticipated that the heterogeneous interfaces between the second phase and the matrix in $\text{Fe}_{50}\text{Mn}_{30}\text{Co}_{10}\text{Cr}_{10}$ HEAs provide effective sinks to trap point defects, including He atoms [1,2], so as to suppress the formation of defect clusters and He bubbles in the matrix. This in turn would improve the irradiation resistance for swelling, irradiation hardening and He embrittlement of a material. Although the coarse-grained HEAs manifest excellent irradiation tolerance, it is still unclear how these HEAs respond, in particular under ion irradiation conditions, when their intrinsic sizes are reduced into the nanoscale, associated with a sharply increased volume fraction of GBs that can serve as defect sinks [25].

In parallel, previous studies demonstrated the introduction of high density of heterogeneous interfaces into a material to form the nanolaminate (NL) can significantly improve its irradiation resistance. For example, numerous studies focused on the irradiation behavior of conventional bimetal NLs, such as FCC/BCC Cu/Nb [26,27], Cu/Mo [28], Cu/V [29] and Ag/V [30], FCC/FCC Cu/Co [31], Cu/Ag [32] and Ni/Ag [33], FCC/HCP Cu/Zr [34], BCC/BCC Fe/W [35], BCC/HCP Mo/Zr [36] and Nb/Zr [37], revealing a trend that more interfaces (or smaller layer thickness h) would lead to less irradiation hardening. A recent study [38] conducted on Cu/Nb NLs through He ion implantation experiments and atomic simulations, and found that the formation of larger He clusters was significantly delayed in the amorphous area near the interface, because such 3D interface had an excessive amount of free volume and high “sink capacity”. The size-dependent radiation hardening has been quantitatively analyzed in above He ion-irradiated nanolayered systems in terms of the average bubble spacing l_{bub} , the diameter d_{bub} and the layer thickness h . The peak strength of irradiated NLs is determined by the inherent interfacial resistance to slip transmission and interactions of dislocations and radiation-induced obstacles (e.g. dislocation loops and He bubbles). Moreover, this nanolaminated design is also a viable pathway to balance the strength-ductility conflict, which confers these ductile nanolayered materials size-driven ultra-high strength, often in a fashion that smaller layer thickness (h) leads to higher strength [34,36,38] and greater strain rate sensitivity (SRS m). Therefore, we expect that when a metal (e.g. Cu) is embedded into the duplex $\text{Fe}_{50}\text{Mn}_{30}\text{Co}_{10}\text{Cr}_{10}$ HEA matrix to synthesize the HEA/Cu NLs, they probably exhibit excellent mechanical properties and extraordinary irradiation tolerance simultaneously, which is largely unknown to date.

In this work, we selected TRIP-DP-HEA (HEA = $\text{Fe}_{50}\text{Mn}_{30}\text{Co}_{10}\text{Cr}_{10}$, FMCC) combined with Cu to form HEA/Cu nano-layered

structure. The HEA/Cu NLs not only have the inherent characteristics of HEAs, but also have abundant heterophase interfaces. For comparison reasons, we also prepared another single phase FCC HEA (i.e., $\text{Fe}_{50}\text{Mn}_{30}\text{Co}_{10}\text{Ni}_{10}$, FMCN), and constructed the $\text{Fe}_{50}\text{Mn}_{30}\text{Co}_{10}\text{Ni}_{10}/\text{Cu}$ NLs under the same conditions to uncover the discrepancies in both mechanical and irradiation behavior between $\text{Fe}_{50}\text{Mn}_{30}\text{Co}_{10}\text{Cr}_{10}/\text{Cu}$ (FMCC/Cu) and $\text{Fe}_{50}\text{Mn}_{30}\text{Co}_{10}\text{Ni}_{10}/\text{Cu}$ (FMCN/Cu) caused by the influence of duplex HEA and the single phase HEA in NLs. Similar to conventional bimetal NLs, both as-deposited and irradiated HEA/Cu (HEA = FMCC, FMCN) NLs showed the trend of “smaller is stronger”. Recent studies found that the irradiation hardening monotonously increases with increasing h in conventional bimetal NLs. However, unexpectedly in the present $\text{Fe}_{50}\text{Mn}_{30}\text{Co}_{10}\text{Cr}_{10}/\text{Cu}$ NLs, the irradiation hardening decreases monotonically with increasing h , while that of the present $\text{Fe}_{50}\text{Mn}_{30}\text{Co}_{10}\text{Ni}_{10}/\text{Cu}$ NLs increases firstly, reaching a peak at a critical h of ~ 50 nm and then decreases with increasing h .

2. Experimental procedure

2.1. Materials preparation

The HEA/Cu (HEA = $\text{Fe}_{50}\text{Mn}_{30}\text{Co}_{10}\text{Cr}_{10}$, $\text{Fe}_{50}\text{Mn}_{30}\text{Co}_{10}\text{Ni}_{10}$, atomic fraction) NLs with a total thickness of 1.5 mm were deposited on (111)-Si substrates by direct current (DC) magnetron sputtering. Pure Cu (99.995%), $\text{Fe}_{50}\text{Mn}_{30}\text{Co}_{10}\text{Cr}_{10}$ (99.95%) and $\text{Fe}_{50}\text{Mn}_{30}\text{Co}_{10}\text{Ni}_{10}$ (99.95%) targets were used to prepare HEA/Cu NLs with equal individual layer thickness (h) in the range of 5–150 nm. The sputtering chamber was evacuated to a base pressure of 4×10^{-4} Pa before the deposition process and 1.0 Pa of Ar pressure was maintained during the preparation process. The purity of Ar is 99.999%. The sputtering process was performed at room temperature. The first layer on the substrate was Cu and the cap layer was HEA. We performed He ion-implantation experiment with a He ion energy of 40 keV and a total fluence of 1×10^{17} ions cm^{-2} by using a BNU-400 ion implanter. The base pressure was maintained at 1×10^{-4} Pa. The He concentration vs. penetration depth curve was simulated by the Stopping and Range of Ions in Matter (SRIM) software using quick calculation mode.

2.2. Microstructural characterization

X-ray diffraction (XRD) experiments were performed at room temperature using a Bruker D8 Discover powder X-ray diffractometer to identify the phase structure and crystallographic orientations. Transmission electron microscopy (TEM) experiments were operated on a JEOL JEM-2100F electron microscope with energy dispersive spectroscopy (EDS) at the 200 kV accelerating voltage to observe the microstructural features of HEA/Cu NLs, such as layer thickness (h) and average grain sizes (d) of constituents, as well as the sizes and distributions of irradiation defects. Following our previous work [28,38], the convergent beam electron diffraction (CBED) technique, which can reach an accuracy of $\sim 5\%$ in determining foil thickness was employed to measure the average TEM foil thickness. This method was also adopted by others [31] to measure the thickness of NL samples.

2.3. Nanoindentation tests

To measure the hardness (H) of the as-deposited and irradiated HEA/Cu NLs, nanoindentation hardness tests were performed on a TI950 TriboIndenter (Hysitron, Minneapolis, MN) equipped with a standard Berkovich diamond indenter with a nominal tip radius of curvature about 50 nm under the load-controlled mode at room

temperature. In the load controlled mode, the strain rate $\dot{\varepsilon}$ is defined by [39]:

$$\dot{\varepsilon} = \frac{\dot{P}}{2P} \quad (1)$$

where \dot{P} is loading rate (mN s^{-1}), $\dot{P} = dP/dt$. The hardness test was conducted on the load-controlled mode for all films under different loading time spanning from 5 to 100 s, correspondingly the loading strain rates ($\dot{\varepsilon}$) spanning from 0.005 s^{-1} to 0.1 s^{-1} , in order to obtain the strain rate sensitivity (SRS) index m . The SRS m is experimentally defined as the double logarithmic plot slope of hardness H and strain rates $\dot{\varepsilon}$ under isothermal conditions, which can be expressed as $m = \frac{\partial \log(H)}{\partial \log(\dot{\varepsilon})}$. The holding time is 2 s, while the unloading time is 5 s. The allowed drift rate was set as 0.01 nm s^{-1} , which is 10 times smaller than the typical value (0.1 nm s^{-1}) to guarantee the reliability and accuracy of the measurements. Each sample would be tested at a minimum of 9 indents separated from each other of $\sim 30 \text{ mm}$ to obtain the average hardness (H) and standard deviations. To reduce the indentation size effects and substrate effects, the indentation depth was usually selected within $\sim 15\%$ of the total thickness of the film materials. In parallel, the bubble gradient effects have little influence on the hardness of HEA/Cu NLs within this indentation depth-range [38]. Therefore, all the hardness values of deposited and irradiated HEA/Cu NLs were measured at about 150 nm via the nanoindentation test.

The He concentration vs. penetration depth profiles calculated by the SRIM could be used for the design of indentation tests [30,40]. Based on the SRIM simulated results, the highest radiation damage was about 4 dpa and the highest He concentration was $\sim 8 \text{ at.\%}$ in HEA/Cu NLs with different h . The maximum He concentration was achieved at the depth of $\sim 150 \text{ nm}$. Although the NLs with more interfaces (when $h < 10 \text{ nm}$) often showed different positions of the peak density of He bubbles between experimental observations and SRIM simulations [31], such a discrepancy in the present HEA/Cu NLs was not notable, consistent with our previous work [36,38].

3. Results

3.1. Crystallographic orientations of HEA/Cu NLs

High-angle XRD spectra for as-deposited and irradiated $\text{Fe}_{50}\text{Mn}_{30}\text{Co}_{10}\text{Cr}_{10}/\text{Cu}$ (termed as FMCC/Cu) and $\text{Fe}_{50}\text{Mn}_{30}\text{Co}_{10}\text{Ni}_{10}/\text{Cu}$ (termed as FMCN/Cu) NLs with h spanning from 5 to 150 nm are shown in Fig. 1(a-c) and (d-f), respectively. In the FMCC/Cu NLs, both Cu and FMCC layers show strong (111) and quite weak (200) textures, while HEA layers additionally show (0002) HCP texture when $h > 10 \text{ nm}$. By contrast, the FMCN/Cu NLs show strong (111), weak (200) and (220) textures. The overlapping peaks of Cu and HEA (HEA = FMCC, FMCN) are ascribed to their same crystal structure and similar lattice parameters. Compared with the as-deposited NLs, after irradiation the angles of peaks have almost no change, while the intensity of all diffraction peaks decrease, as shown in Fig. 1(c) and (f).

3.2. Internal microstructure of un-irradiated HEA/Cu NLs

3.2.1. As-deposited HEA/Cu NLs

Fig. 2 displays typically cross-sectional TEM images of as-deposited FMCC/Cu and FMCN/Cu NLs with different h , respectively. It is found that the internal morphologies of microstructure can be divided into two regimes by the critical layer thickness h_c . The main results are summarized as follows:

(i) In the Regime-I with $h < h_c$, the HEA/Cu interfaces cannot be identified in the bright-field TEM images and a columnar grain along the growth direction contains several interfaces, while these

STEM images display clearly nanolayered structure, as shown in Fig. 2(a) and (e). The selected area diffraction patterns (SADPs) in Fig. 2(a) and (e) show the overlapping diffraction rings and single FCC structure of these two HEA/Cu NLs, which are in accordance with the XRD peaks. One can find that the observed layer interfaces are coherent without misfit dislocations, as shown in Fig. 2(b) and (f) for FMCC/Cu and FMCN/Cu NLs, respectively. Besides, some nanotwins that penetrated across the interface can be observed in both Cu and HEA layers in this size regime. The average twin thickness and the twin's fraction in the present HEA/Cu NLs are listed in Table 1. Corresponding TEM images for FMCC/Cu and FMCN/Cu NLs are presented in Fig. S1 in Supplementary Material.

(ii) In the Regime-II with $h \geq h_c$, the modulation structure and interfaces are clear in TEM images and grains are confined within the isolated layers, as shown in Fig. 2(c, d) for FMCC/Cu NLs and Fig. 2(g, h) for FMCN/Cu NLs. For FMCC/Cu NLs, the HCP phase appears in FMCC layers, as verified by the overlapping (111)_F and (0002)_H diffraction rings and individual HCP (1013)_H rings, see Fig. 2(c) for $h = 100 \text{ nm}$ samples. Meanwhile, the Fast Fourier Transformation (FFT) images also manifest the dual-phase structure of FMCC layers. By contrast, the FMCN/Cu NLs in the Regime-II exhibit the single FCC structure, as shown in Fig. 2(g). Moreover, the HRTEM images manifest that the observed interfaces are coherent, and the Burgers circuit near the interfaces are perfect without misfit dislocations, see Fig. 2(h). Also, some nanotwins confined into the isolated Cu layers can be observed in this size regime.

3.2.2. Deformed microstructure of as-deposited HEA/Cu NLs

Post-mortem TEM observations were performed on the indented $h = 25 \text{ nm}$ HEA/Cu NLs to reveal the deformation behavior and underlying mechanisms, as shown in Fig. 3. The constituent layers of both Cu and HEAs behave homogenous thinning under the indenter tip without any localized shear bands in the present two kinds of HEA/Cu NLs, as shown in Fig. 3(a, e). Fig. 3(b) shows that in FMCC/Cu NLs with $h = 25 \text{ nm}$, the HCP {1013}_H ring disappears after deformation, indicating the phase transformation from HCP to FCC occurs in the FMCC layers, as supported by the SADPs. Nanotwins still exist in both Cu and HEAs layers after indentation, as indicated by arrows in Fig. 3(c), implying they are stable during deformation. For the FMCN/Cu NLs, the SADP of the indented sample is the same as the as-deposited one, as shown in Fig. 3(f). It proves that the indented samples remain the single phase FCC structure. This is likely because the FCC-to-HCP phase transformation is reversible and occurs in a very short time, as uncovered by recent atomistic simulations [22]. Also, the nanotwins in both Cu and FMCN layers can be observed after indentation, see Fig. 3(g, h).

3.3. Internal microstructure of He ion-irradiated HEA/Cu NLs

3.3.1. Initial microstructure of irradiated HEA/Cu NLs

Fig. 4(a) displays the cross-sectional TEM image of He ion-irradiated FMCC/Cu NLs with $h = 100 \text{ nm}$. The nanolayered structure can be clearly discerned, and an SADP of the irradiated region confirms the coherent interface between Cu and FMCC, which rises from the same lattice structure (FCC) and the similar lattice parameters (Cu~0.3615 nm, FMCC~0.3580 nm, FMCN~0.3590 nm). The superimposed solid curve presents the depth profile of He concentrations calculated by SRIM. In the peak damage region, a high density of He bubbles was observed in both FMCC and Cu layers, as shown in Fig. 4(b, c). These He bubbles are randomly distributed in Cu and FMCC layers, appearing as white and small-sized dots. Moreover, the HCP phase in FMCC still exists after He-implantation, as verified by the FFT analysis of a boxed region in Fig. 4(d1). Also, the coherent FMCC/Cu interface and the FCC/HCP phase boundary

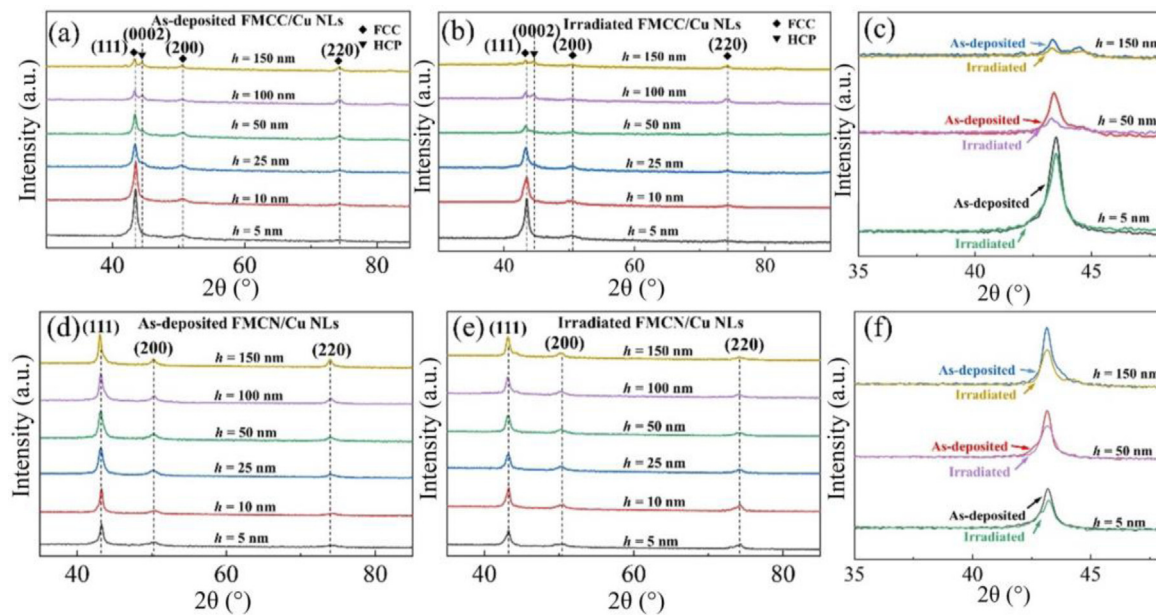


Fig. 1. XRD patterns for $\text{Fe}_{50}\text{Mn}_{30}\text{Co}_{10}\text{Cr}_{10}/\text{Cu}$ and $\text{Fe}_{50}\text{Mn}_{30}\text{Co}_{10}\text{Ni}_{10}/\text{Cu}$ NLs with different layer thicknesses h : (a, d) before irradiation; (b, e) after irradiation. (c, f) A comparison of XRD profiles between as-deposited and irradiated HEA/Cu NLs.

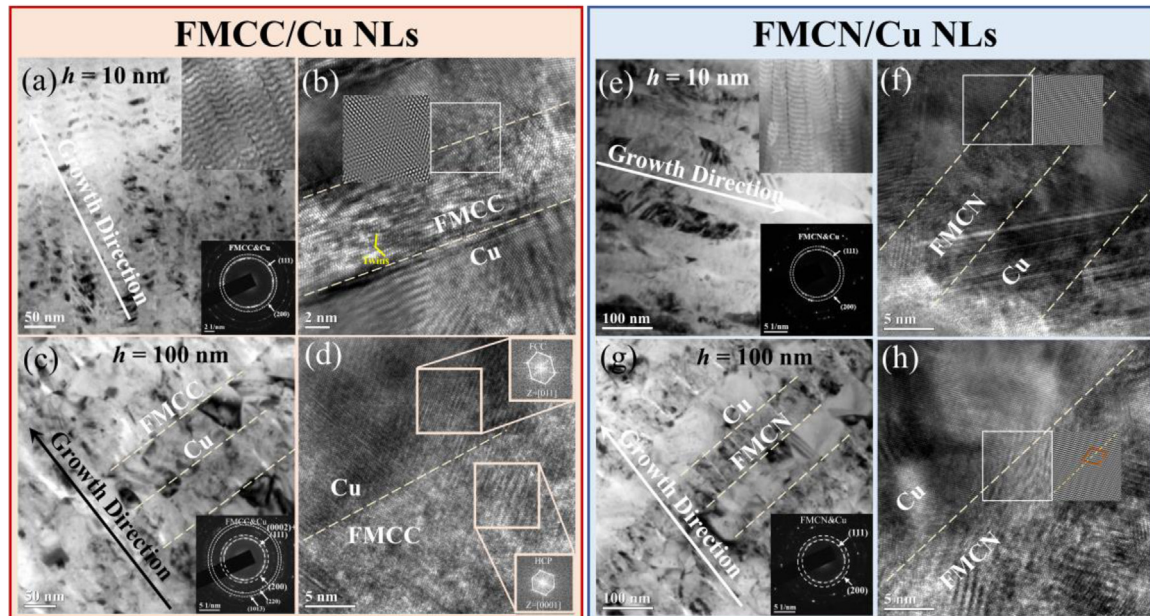


Fig. 2. Typically cross-sectional TEM images of (a, b) $h = 10$ nm and (c, d) $h = 100$ nm $\text{Fe}_{50}\text{Mn}_{30}\text{Co}_{10}\text{Cr}_{10}/\text{Cu}$ NLs and (e, f) $h = 10$ nm and (g, h) $h = 100$ nm $\text{Fe}_{50}\text{Mn}_{30}\text{Co}_{10}\text{Ni}_{10}/\text{Cu}$ NLs. The corresponding SADPs are inserted in (a, c, e, g). (b, d) HRTEM images show coherent interfaces, while the corresponding FFT image of the boxed regions in (d) displays the HCP phase in FMCC layers. (f, h) HRTEM images show the coherent interface between Cu and FMCN layers. The STEM images inserted in (a, e) show modulated nanolayered structure.

Table 1
Statistical result of twin thickness and twin's fraction in FMCC/Cu and FMCN/Cu NLs.

h (nm)	FMCC/Cu NLs				FMCN/Cu NLs			
	Twin's fraction P^T (%)		Twin thickness l_T (nm)		Twin's fraction P^T (%)		Twin thickness l_T (nm)	
	P^T_{all}	P^T_{Cu}	l_{all}	l_{Cu}	P^T_{all}	P^T_{Cu}	l_{all}	l_{Cu}
5	62.5 ± 3.1	-	5.3 ± 1.8	-	71.7 ± 4.5	-	5.5 ± 1.5	-
10	60.4 ± 4.9	-	5.1 ± 1.5	-	71.5 ± 5.7	-	5.6 ± 1.3	-
25	-	40.6 ± 2.1	-	5.5 ± 1.4	72.8 ± 3.1	-	5.2 ± 1.8	-
50	-	48.9 ± 3.1	-	7.6 ± 1.8	-	50.3 ± 2.3	-	8.3 ± 2.1
100	-	50.7 ± 4.0	-	8.0 ± 1.3	-	54.8 ± 5.9	-	10.9 ± 1.6
150	-	51.4 ± 2.3	-	9.5 ± 1.8	-	56.1 ± 3.6	-	11.2 ± 1.2

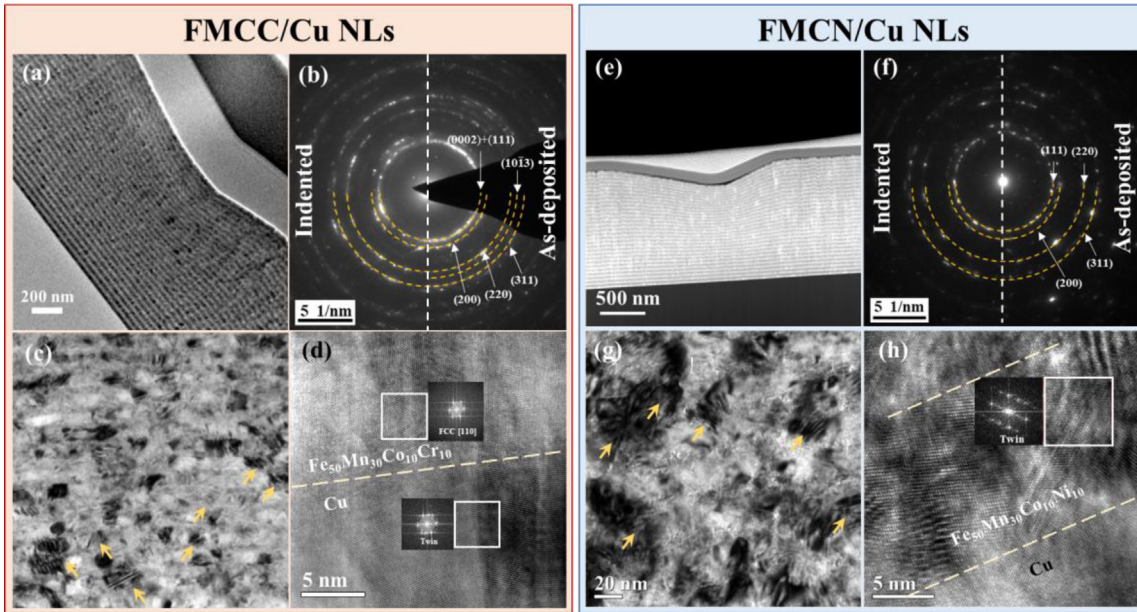


Fig. 3. (a, e) Representative STEM images of the deformed microstructure underneath the indenter in the as-deposited $\text{Fe}_{50}\text{Mn}_{30}\text{Co}_{10}\text{Cr}_{10}/\text{Cu}$ and $\text{Fe}_{50}\text{Mn}_{30}\text{Co}_{10}\text{Ni}_{10}/\text{Cu}$ NLs with $h = 25 \text{ nm}$. (b, f) The SADPs of indented (on the left) and as-deposited (on the right) samples. (c, g) Typical TEM images of the deformed microstructure underneath the indenter with twins indicated by arrows. (d, h) Typical HRTEM images of the indented region, showing the presence of nanotwins after deformation.

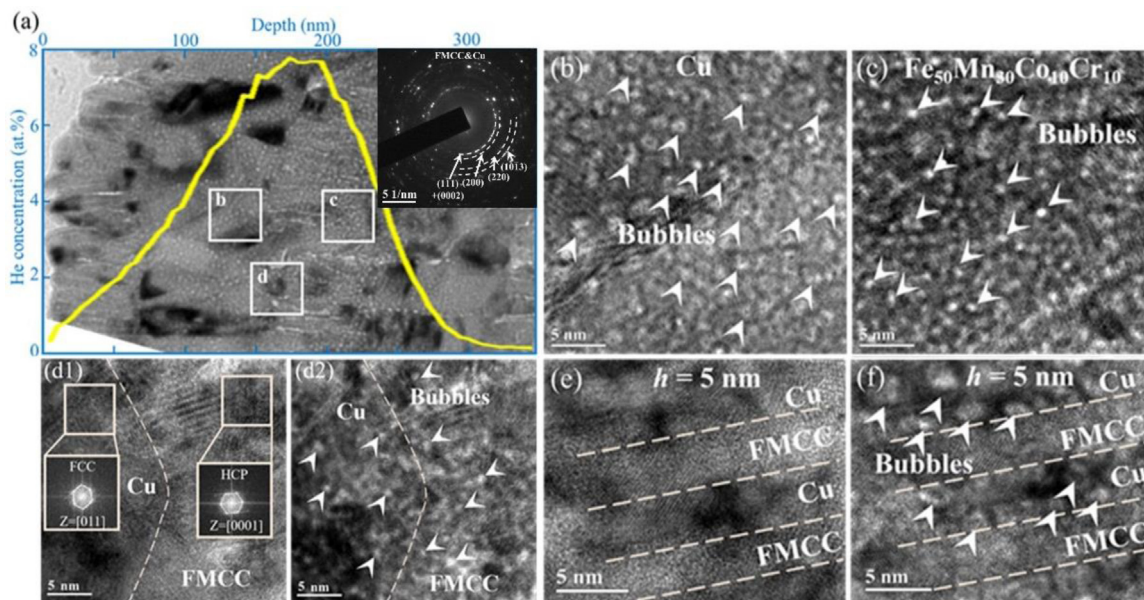


Fig. 4. (a) Cross-sectional TEM image for $\text{Fe}_{50}\text{Mn}_{30}\text{Co}_{10}\text{Cr}_{10}/\text{Cu}$ NLs with $h = 100 \text{ nm}$ after He irradiation. The SADP of the irradiated region shows the unchanged crystallographic orientation of the two constituents. Superimposed on image (a) is the He concentration vs. penetration depth profile simulated by SRIM. (b-d2) Magnified views of the irradiated boxed regions in (a) show the distribution of He bubbles indicated by white arrows. The corresponding FFT image of the boxed regions in (d1) shows the HCP phase in FMCC layers. Images (e) and (f) show the distribution of He bubbles of $h = 5 \text{ nm}$ samples. Images (d1, e) are captured in the condition of under-focus 0 nm and images (b, c, d2, f) are captured in the condition of under-focus 250 nm to clearly show the He bubbles.

are decorated with bubbles, as shown in Fig. 4(d2). As shown in Fig. 4(e, f), He bubbles are only distributed in Cu layers and no bubbles emerge in FMCC layers, when h is reduced down to $\sim 5 \text{ nm}$. Under the current He ion-irradiation condition, the nanotwins are survived in FMCC/Cu NLs.

For comparison, the microstructure of irradiated FMCN/Cu NLs with $h = 100 \text{ nm}$ was also examined. Fig. 5(a) shows a panoramic view of the irradiated specimen incorporating the SRIM simulated depth-dependent profile of He concentrations. The boxed regions captured at different depths are shown to uncover the distribu-

tion of He bubbles. In Cu layers, He bubbles were randomly distributed, see Fig. 5(b), appearing as clearly defined circles. In the peak damage region of FMCN layers, a high density of He bubbles are present in the form of small and obscure white dots, see Fig. 5(c). Specifically, it is found that in irradiated Cu layers numerous bubble chains are arranged at GBs in $h = 150 \text{ nm}$ samples, as shown in Fig. 5(d). Similar to the case of $h = 5 \text{ nm}$ FMCC/Cu NLs, these He bubbles are only distributed in Cu layers, as shown in Fig. 5(e). Still, the nanotwins are survived in FMCN/Cu NLs under the current He ion-irradiation condition.

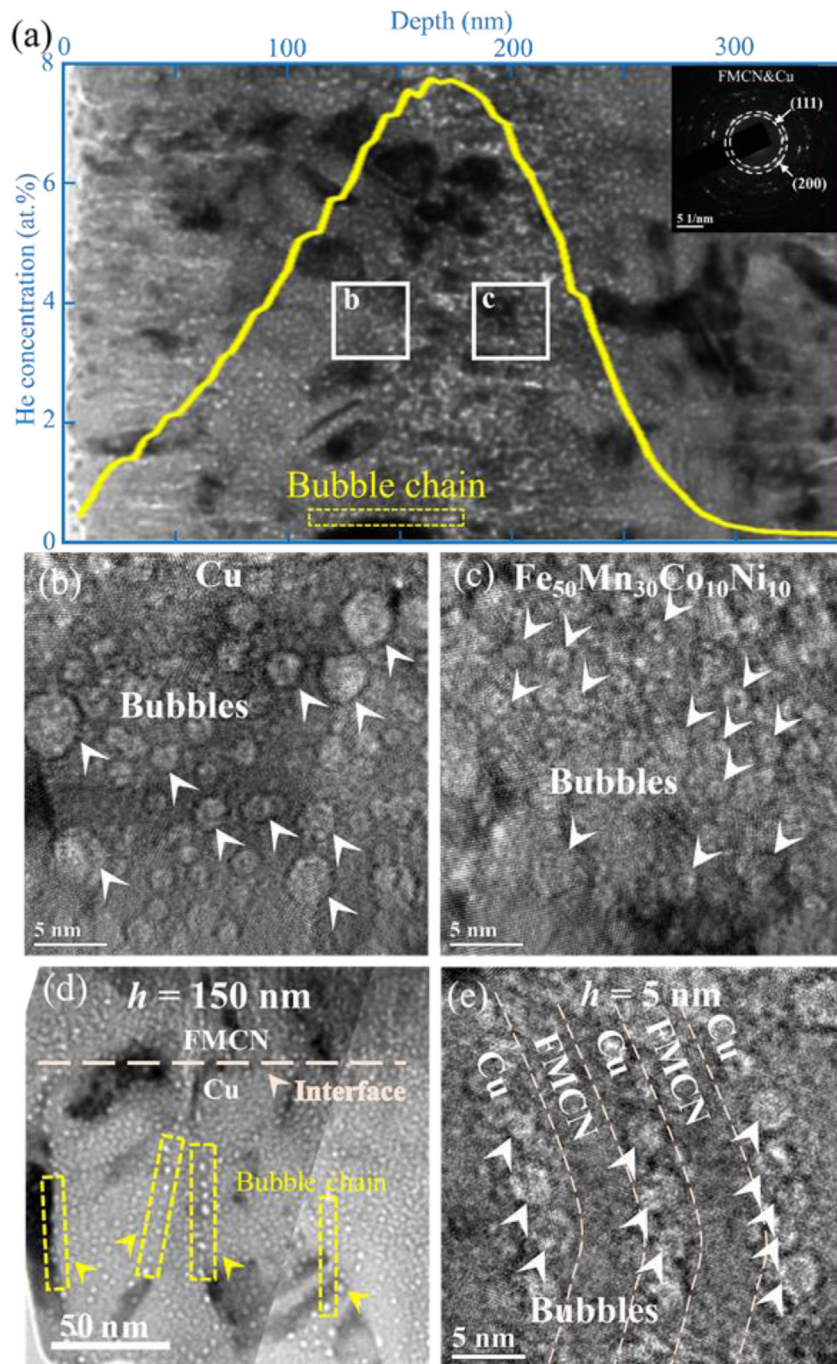


Fig. 5. (a) A cross-sectional TEM image of irradiated $\text{Fe}_{50}\text{Mn}_{30}\text{Co}_{10}\text{Ni}_{10}/\text{Cu}$ NLs of $h = 100$ nm with embedded He concentration profile. The corresponding SADP inserted in (a) exhibits (111) and (200) textures after irradiation. (b, c) HRTEM images of the boxes b and c labeled in (a) at different penetration depths, showing bubbles are randomly distributed in Cu and FMCN layers. (d) A TEM image of irradiated $\text{Fe}_{50}\text{Mn}_{30}\text{Co}_{10}\text{Ni}_{10}/\text{Cu}$ NLs $h = 150$ nm showing numerous bubble chains at grain boundary in Cu, as indicated by arrows. (e) A HRTEM image shows the distribution of He bubbles in $h = 5$ nm samples.

3.3.2. Deformed microstructure of irradiated HEA/Cu NLs

The microstructure of irradiated $h = 25$ nm HEA/Cu NLs after nanoindentation was examined, as shown in Fig. 6. Similar to the indented as-deposited sample, there is also no shear banding in the deformed region for these two kinds of NLs, as displayed in Fig. 6(a, e). It appears that the HCP $\{10\bar{1}3\}_\text{H}$ ring disappears after deformation, implying the HCP-to-FCC phase transformation takes place in FMCC layers, see Fig. 6(b). Compared with the indented as-deposited samples, one can claim that He-ion irradiation has no effect on the phase transformation behavior in FMCC HEAs in this work. By contrast, for the FMCN/Cu NLs, the SADP of indented ir-

radiated sample is the same as the as-deposited one, as shown in Fig. 6(f). It means that the indented samples remain the single FCC structure. Also, nanotwins suffered from He-ion irradiation are stable in both Cu and FMCN layers after indentation, see Fig. 6(c, g). These small bubbles remain the shape of small white dots, as same as those of undeformed regions, as shown in Fig. 6(d, h).

3.3.3. He bubble size and distribution in irradiated HEA/Cu NLs

Based on the above TEM observations, there are notable discrepancies in shapes and sizes of He bubbles in two constituents. Detailed examinations of He bubble sizes and distributions were

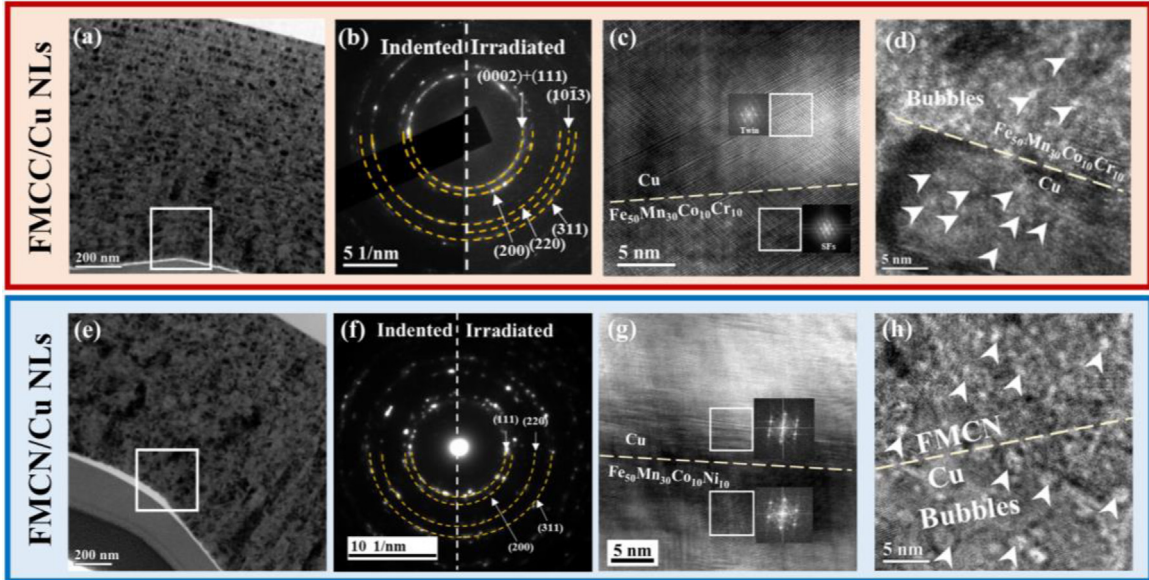


Fig. 6. Representative TEM images of the deformed microstructure underneath the indenter in (a) $\text{Fe}_{50}\text{Mn}_{30}\text{Co}_{10}\text{Cr}_{10}/\text{Cu}$ and (e) $\text{Fe}_{50}\text{Mn}_{30}\text{Co}_{10}\text{Ni}_{10}/\text{Cu}$ NLS with $h = 25 \text{ nm}$ after irradiation. (b, f) Typical SADPs of the indented (on the left) and irradiated (on the right) samples. (c, g) Typical HRTEM images of the indented regions, showing the presence of nanotwins after deformation. (d, h) Typical HRTEM images of the indented regions, showing the He bubbles.

performed on the irradiated HEA/Cu NLS at the irradiation depth of $\sim 150\text{--}200 \text{ nm}$. Because the constituents of HEA/Cu NLS show synergistic deformation behavior, it is necessary to count the He bubble size of Cu and HEA layers to investigate the irradiation tolerance of HEA/Cu NLS. A previous study [30] counted the average He bubbles with the diameter d_{bub} by associating the corresponding defocus with the measured size. It is worth mentioning that one bright dot is not equal to one bubble in the TEM image because of the overlapping of projected bubble images along the TEM foil thickness. Thus, following this method, a sample should be tilted with different angles to estimate the bubble density.

As for FMCC/Cu NLS, the average diameter (d_{bub}) and the average spacing (l_{bub}) of He bubbles in Cu layers are shown in Fig. 7(a). Corresponding TEM images for statistics are presented in Fig. S2 in Supplementary Material. In Cu layers, d_{bub} increases from ~ 1.3 to $\sim 1.5 \text{ nm}$ with reducing h , and l_{bub} slightly increases from ~ 2.7 to $\sim 2.9 \text{ nm}$ as h decreases from 150 to 5 nm. Correspondingly, the He bubble density $N_{\text{bub}} \approx 1/(l_2 \text{bub} d_{\text{bub}})$ in Cu layers shows a remarkably decreased trend with reducing h , see Fig. 7(c). By contrast, d_{bub} and l_{bub} in FMCC layers are smaller than those in Cu layers, as shown in Fig. 7(b). Since it is difficult to observe He bubbles in FMCC layers with $h = 5 \text{ nm}$, only the sizes of bubbles in FMCC layers with $h = 10, 25, 50, 100$ and 150 nm were counted (and discussed below). It is interesting to find that d_{bub} is almost a constant of $\sim 0.8 \text{ nm}$, regardless of h . While l_{bub} in FMCC layers remains at $\sim 2.7 \text{ nm}$ with reducing h from 150 to 10 nm, somewhat smaller than/approaching to that in Cu layers. Accordingly, N_{bub} in FMCC layers is increased by ~ 1.2 times as h increases from 10 to 150 nm, far higher than that in Cu, see Fig. 7(d).

Similarly, the statistical results of FMCN/Cu NLS are presented in Fig. 8. Corresponding TEM images for statistics are presented in Fig. S3. In Cu layers, d_{bub} increases from ~ 1.8 to $\sim 2.2 \text{ nm}$, and also l_{bub} monotonically increases from ~ 3.5 to $\sim 3.8 \text{ nm}$ as h is reduced, as shown in Fig. 8(a). Correspondingly, $N_{\text{bub}} \approx 1/(l_2 \text{bub} d_{\text{bub}})$ in Cu layers presents a notably decreased trend with reducing h , see Fig. 8(c). Still, d_{bub} and l_{bub} of He bubbles in FMCN layers are much smaller than those in Cu layers, as shown in Fig. 8(b). It appears that the size h -independent d_{bub} and l_{bub} in FMCN layers are nearly constant of $\sim 1.4 \text{ nm}$ and $\sim 2.9 \text{ nm}$, respectively. Accordingly, N_{bub} slightly increases as h increases from 10 to 150 nm. Furthermore,

comparing Fig. 7 and Fig. 8, one can argue that under the same irradiation condition, the average bubble sizes of both Cu and HEA layers in FMCN/Cu NLS are larger than those in FMCC/Cu NLS, implying FMCC/Cu NLS have better irradiation resistance.

The swelling value can be calculated from HRTEM images by the equation [8]: $\chi_s (\%) = \frac{\frac{\pi}{6} \sum_{i=1}^N d_{\text{bub}}^3}{A \times \delta - \frac{\pi}{6} \sum_{i=1}^N d_{\text{bub}}^3}$, where χ_s is the swelling value, A is the image area, δ is the measured TEM foil thickness of $\sim 100 \text{ nm}$, d_{bub} is the average He bubble size, N is the number of He bubble. The irradiation swelling of each layer can be calculated within the depth of $\sim 100\text{--}200 \text{ nm}$, and then the overall irradiation swelling of HEA/Cu NLS can be obtained by summing the swelling of each layer. It is worth mentioning that, taking the $h = 50 \text{ nm}$ sample as an example, the irradiation swelling contribution of Cu is 0.07%, while the contribution of FMCC is 0.02% in FMCC/Cu NLS. Similarly, in the FMCN/Cu NLS, the contribution of Cu is 0.091%, while the contribution of FMCN is 0.056%. It is obvious that the contribution of HEA layer is much lower. Fig. 9 shows the variation in He bubble-induced swelling as a function of the layer thickness h . It is found that overall both FMCC/Cu and FMCN/Cu NLS manifest the reduced swelling propensity with decreasing h . For the FMCC/Cu NLS, the swelling is ranging from 0.069% to 0.010% while that of FMCN/Cu NLS is ranging from 0.097% to 0.149%. Thus, the FMCC/Cu NLS display more excellent resistance against swelling than the FMCN/Cu samples.

3.4. Mechanical properties of HEA/Cu NLS

3.4.1. Nanoindentation hardness of HEA/Cu NTNLs

The typical indentation load-depth curves of both as-deposited and irradiated HEA/Cu NLS with different h at the same strain rate of 0.05 s^{-1} are displayed in Fig. 10(a-d). It is found that the indentation depth of both as-deposited and irradiated HEA/Cu NLS decreases with reducing h from 150 to 5 nm, as shown in Fig. 10(a, b) for FMCC/Cu NLS and Fig. 10(c, d) for FMCN/Cu NLS. Moreover, compared with the as-deposited samples at a given h , the irradiated ones have a smaller indentation depth caused by the irradiation hardening after He ion-implantation.

In coincidence with the microstructure transition, the measured hardness H of the present HEA/Cu NLS also displays the unique size

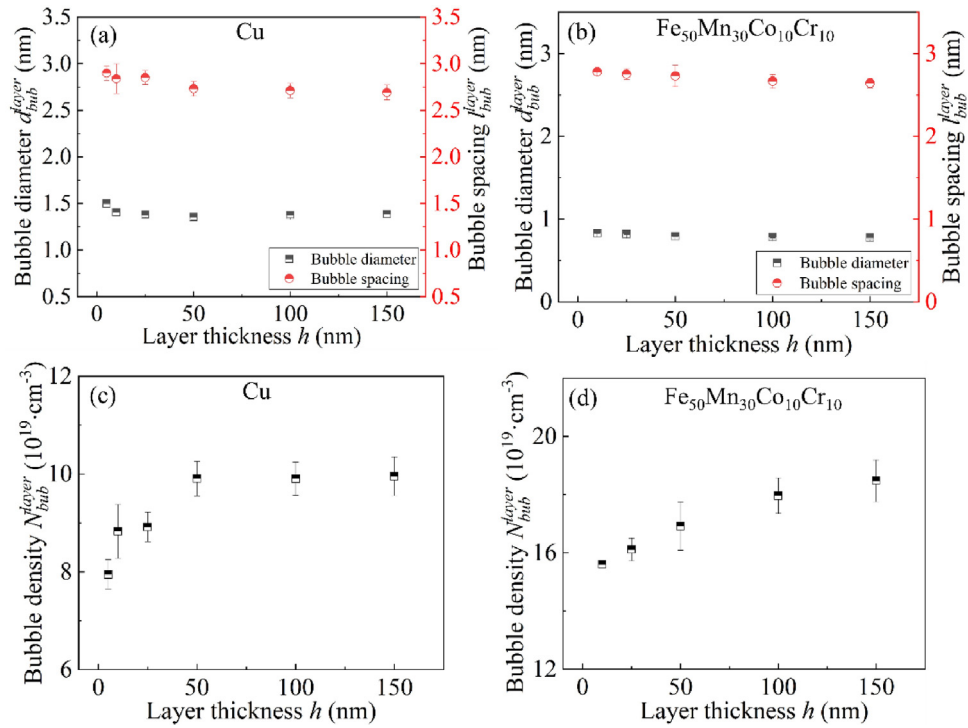


Fig. 7. Statistical results on He bubbles in irradiated $\text{Fe}_{50}\text{Mn}_{30}\text{Co}_{10}\text{Cr}_{10}/\text{Cu}$ NLs. The average bubble diameter and bubble spacing, bubble density as a function of h in Cu layer (a, c) and in FMCC layer (b, d) respectively.

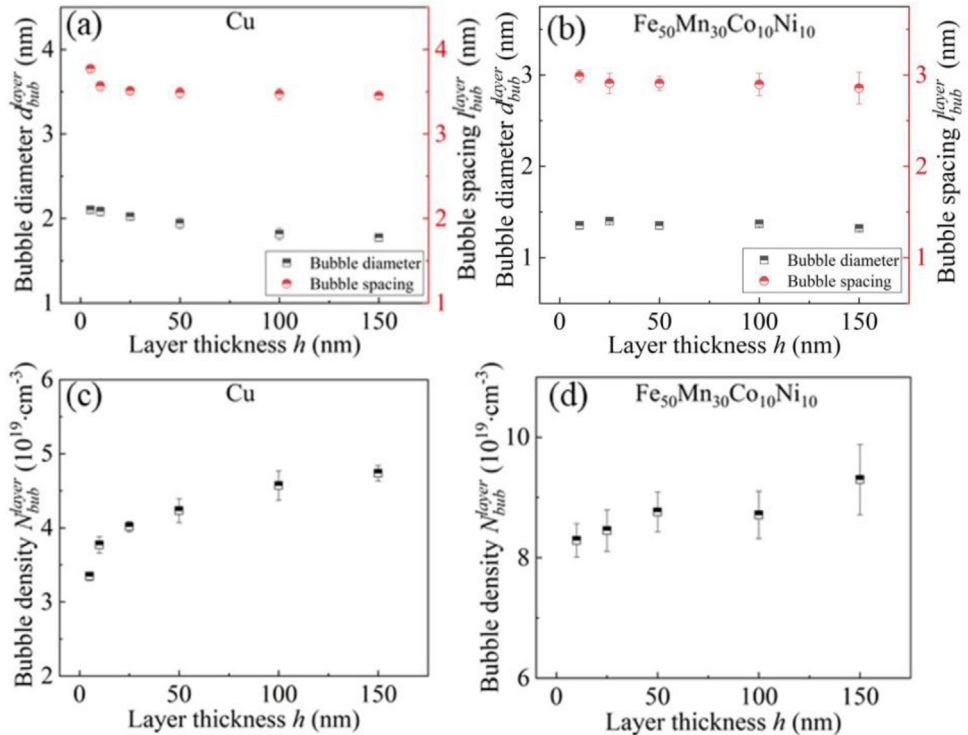


Fig. 8. Statistical results on the parameters of He bubbles in the irradiated $\text{Fe}_{50}\text{Mn}_{30}\text{Co}_{10}\text{Ni}_{10}/\text{Cu}$ NLs. The average bubble diameter and bubble spacing, bubble density as a function of h in Cu layer (a, c) and in FMCN layer (b, d), respectively.

h -dependent behavior in Regimes I and II, respectively. It seems that for the as-deposited FMCC/Cu NLs, the hardness H increases from ~ 3.9 to ~ 4.7 GPa with reducing h from 50 to 5 nm in the Regime-I. In the Regime-II with large h , the FMCC/Cu NLs show a size h -independent hardness plateau of ~ 3.8 GPa (~ 1.0 GPa higher than that of monolithic FMCC thin films). By contrast, the hard-

ness H of irradiated samples monotonically increases from ~ 4.3 to ~ 5.6 GPa with reducing h , as shown in Fig. 11(a), indicative of pronounced irradiation hardening after He ion-implantation. Moreover, it is found that the irradiation hardening or the hardness increment decreases from ~ 0.8 to ~ 0.45 GPa with increasing h from 5 to 150 nm, as shown in Fig. 11(b).

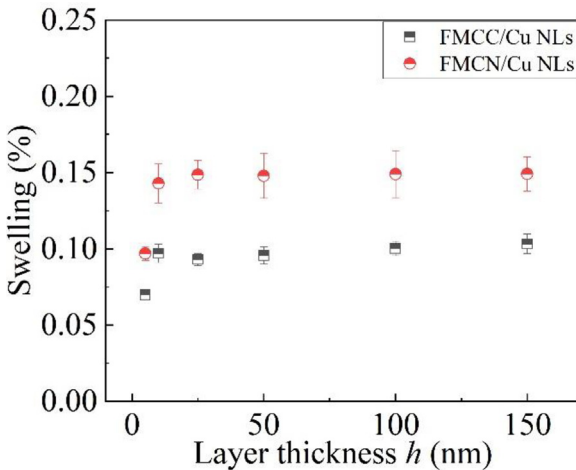


Fig. 9. Swelling is estimated based on the bubble densities and sizes. In the FMCC/Cu NLs, the magnitude of swelling increases with increasing h . In the FMCN/Cu NLs, the magnitude of swelling increases with h increasing from 5 nm to 25 nm. When $h \geq 50$ nm, swelling does not change significantly.

Compared with the as-deposited FMCC/Cu NLs, a similar phenomenon was observed in their FMCN/Cu siblings. That is to say, in the Regime-I with small h , the hardness H increases from ~ 3.9 to ~ 4.6 GPa with h reducing from 50 to 5 nm, while in the Regime-II, the FMCN/Cu NLs also show a hardness plateau ~ 3.8 GPa (equal to that of hard monolithic FMCN thin films), as shown in Fig. 11(c). After He ion irradiation, the hardness H of FMCN/Cu NLs monotonically increases from ~ 4.3 to ~ 5.3 GPa with reducing h , as shown in Fig. 11(c). Unexpectedly, one can find that the irradiation hardening increases first with decreasing h , reaching a peak value of 0.92 GPa at a critical size $h = 50$ nm, above which the irradiation hardening decreases with further increasing h , see Fig. 11(d).

Finally, a comparison of the irradiation hardening behavior between the present HEA/Cu NLs and previously reported conventional bimetal NLs, such as Mo/Cu [28], V/Cu [29], V/Ag [30], Ni/Ag [33], Cu/Zr [34], Mo/Zr [36] and Nb/Zr [37] NLs, is shown in Fig. 12. Although the present as-deposited and irradiated samples exhibit the fashion that smaller h results in higher hardness, both FMCC/Cu and FMCN/Cu NLs exhibit unusual irradiation hardening behavior. In other words, the former manifests the increased irradiation hardening with reducing h , while the latter manifests a peak irradiation hardening at a critical size $h \sim 50$ nm, as shown in Fig. 12. These suggested that the irradiation hardening of the present HEA/Cu NLs is far different from that of the reported bimetal NLs associated with reduced irradiation hardening with reducing h . In addition, the present HEA/Cu NLs exhibit greater irradiation hardening at extremely smaller h (< 10 nm) and smaller irradiation hardening at larger h (> 100 nm), compared with conventional bimetal NLs.

3.4.2. Strain rate sensitivity of HEA/Cu NLs

Fig. 13(a) and (b) presents the strain rate-dependent hardness of FMCC/Cu NLs and FMCN/Cu NLs, respectively, before and after He-implantation. The slope of the strain rate-hardness represents the SRS index m , as summarized in Fig. 13(c) and (d). It appears that with decreasing h , the SRS m of as-deposited FMCC/Cu NLs decreases from 0.035 at $h = 150$ nm to 0.007 at $h = 5$ nm. After He-ion irradiation, the FMCC/Cu NLs exhibit reduced SRS from 0.01 to 0.002 with h decreasing from 150 to 10 nm, even becoming negative at $h = 5$ nm, as shown in Fig. 13(c). By contrast, the as-deposited FMCN/Cu NLs exhibit negative SRS m , which decreases from ~ 0 to -0.026 with h decreasing from 150 to 5 nm, as shown in Fig. 13(d). However, after irradiation, the FMCN/Cu NLs show enhanced SRS m that transits from positive SRS ~ 0.003 to negative SRS -0.005 , just opposite to the case of their FMCC/Cu sibling. It should be pointed out that the SRS m of the present

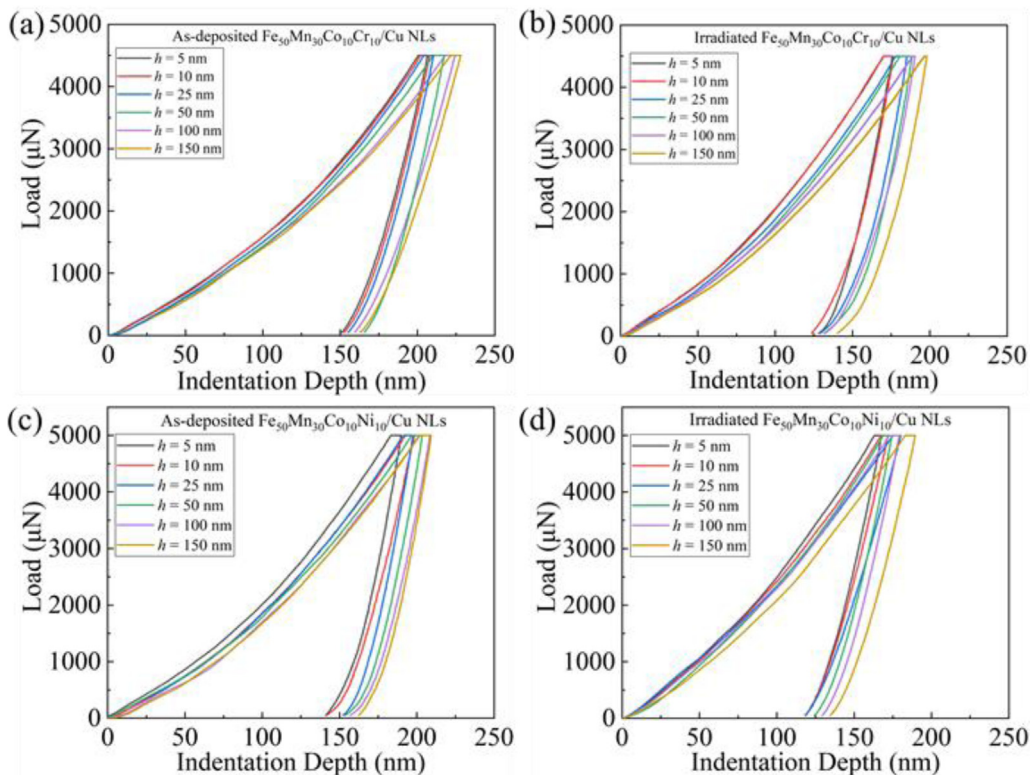


Fig. 10. (a, c) The load-depth curves of as-deposited $\text{Fe}_{50}\text{Mn}_{30}\text{Co}_{10}\text{Cr}_{10}/\text{Cu}$ and $\text{Fe}_{50}\text{Mn}_{30}\text{Co}_{10}\text{Ni}_{10}/\text{Cu}$ NLs at the same strain rate of 0.05 s^{-1} with different h , respectively; (b, d) the load-depth curves of irradiated $\text{Fe}_{50}\text{Mn}_{30}\text{Co}_{10}\text{Cr}_{10}/\text{Cu}$ and $\text{Fe}_{50}\text{Mn}_{30}\text{Co}_{10}\text{Ni}_{10}/\text{Cu}$ NLs with different h , respectively.

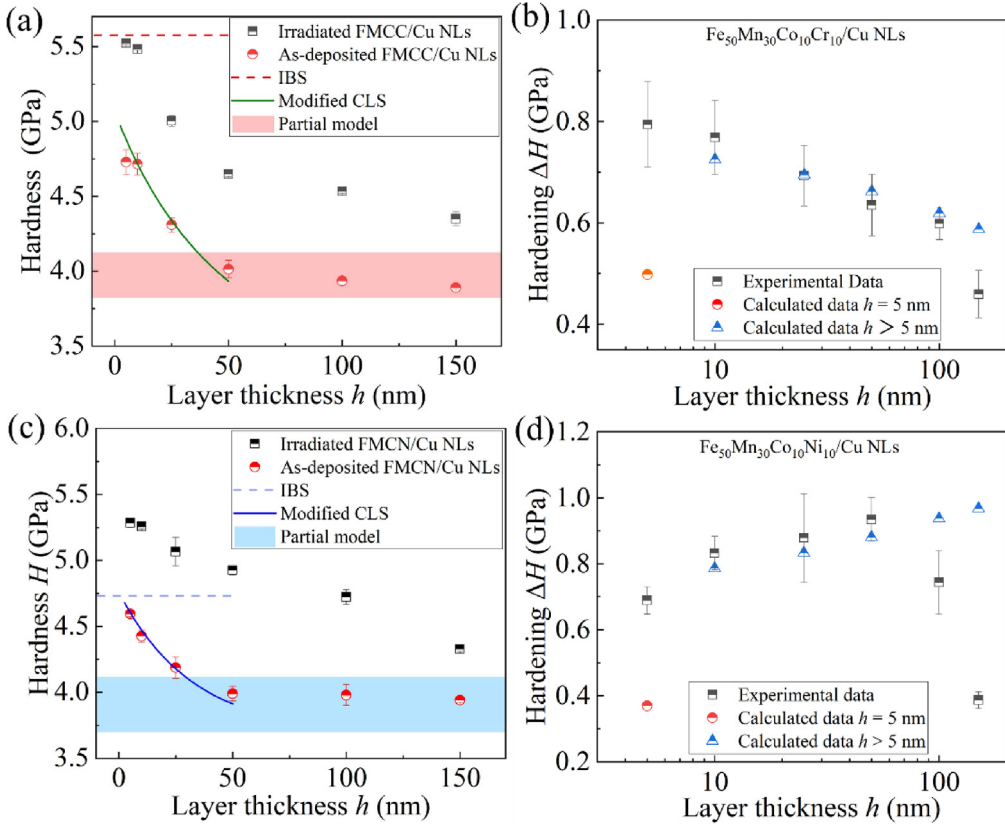


Fig. 11. The measured hardness H as a function of h for (a) $\text{Fe}_{50}\text{Mn}_{30}\text{Co}_{10}\text{Cr}_{10}/\text{Cu}$ and (c) $\text{Fe}_{50}\text{Mn}_{30}\text{Co}_{10}\text{Ni}_{10}/\text{Cu}$ NLs. Calculations on the h -dependent irradiation hardening from different mechanistic models are depicted for (b) $\text{Fe}_{50}\text{Mn}_{30}\text{Co}_{10}\text{Cr}_{10}/\text{Cu}$ and (d) $\text{Fe}_{50}\text{Mn}_{30}\text{Co}_{10}\text{Ni}_{10}/\text{Cu}$ NLs. More details can be referred to in the text.

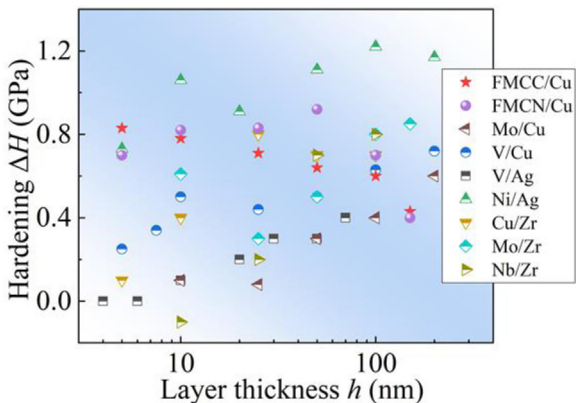


Fig. 12. A comparison of the irradiation hardening as a function of h among the present $\text{Fe}_{50}\text{Mn}_{30}\text{Co}_{10}\text{Cr}_{10}/\text{Cu}$ NLs, $\text{Fe}_{50}\text{Mn}_{30}\text{Co}_{10}\text{Ni}_{10}/\text{Cu}$ NLs and other reported NLs systems Mo/Cu [28], V/Cu [29], V/Ag [30], Ni/Ag [33], Cu/Zr [34], Mo/Zr [36] and Nb/Zr [37] NLs with different interfacial structures.

HEA/Cu NLs before and after He-ion irradiation is far larger than those of monolithic HEA thin films, i.e., ~ 0.036 for FMCC films and ~ 0.024 for FMCN films, but smaller than that of nanocrystalline Cu often in the range of ~ 0.03 to 0.1 [41].

4. Discussion

4.1. The interface density effects on the He ion-irradiation-induced damage

The bubble density N_{bub} in conventional bimetal NLs often increases with increasing h after He ion irradiation. This phe-

nomenon can be ascribed to that the interfaces which serve as effective defect sinks can trap and annihilate irradiation-induced defects without significant irradiation-induced intermixing [42,43]. Because the solid solubility of He in coarse-grained metals is very low, He atoms tend to combine with vacancy clusters and then nucleate and grow into He bubbles. Actually, nanolaminates with smaller h are more effective to manipulate He atoms, because interfaces and misfit dislocations can serve as good defect traps. Thus, the size h -dependent reduction in N_{bub} can be observed in these He ion irradiated HEA/Cu NLs as well as in conventional bimetal systems mentioned above.

Apart from the size h -dependent bubble density N_{bub} explained above, another two striking findings would be elucidated as below. The first one is that although Cu and FMCC layers have similar sizes of bubbles in FMCC/Cu NLs, a different scenario emerges in FMCN/Cu NLs: unlike the constituent Cu with large bubble sizes d_{bub} (~ 2 nm), the small bubble sizes d_{bub} in FMCN layers ($h \geq 10$ nm) are nearly constant on the order of ~ 1.4 nm. Even no He bubbles are observed in the $h = 5$ nm FMCN layers. The underlying reason can be rationalized as follows. The fundamental difference between bubble formation in HEA and Cu is that the motion mode of interstitial defect cluster changes from a long-range 1D mode in pure metals to a short-range 3D mode in HEAs. In addition, the short-range 3D motion of the interstitial clusters greatly increases the probability of interstitial atoms and vacancies recombining [5,6]. Compared with Cu, the cascade in HEAs generates fewer vacancies during He ion-implantation, rendering the vacancies in HEAs become more difficult to gather to form He bubbles, and at ambient temperature, the growth of He bubbles is much slower due to the lower mobility of He atoms in HEAs [25]. Therefore, Cu layers have larger He bubbles with a larger spacing, while HEA layers have smaller bubbles with a smaller spacing. Besides,

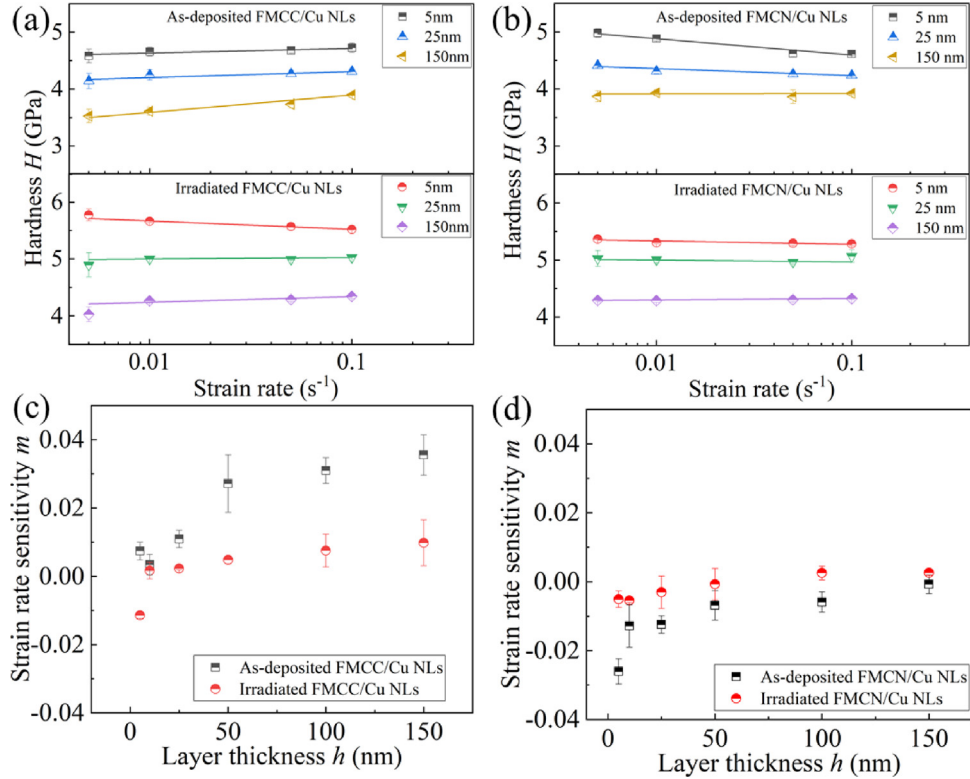


Fig. 13. The measured hardness H as a function of strain rate for (a) as-deposited and irradiated FMCC/Cu NLs with different h and (b) as-deposited and irradiated FMCN/Cu NLs with different h . The slope of each line represents the strain rate sensitivity index m . The strain rate sensitivity m of (c) FMCC/Cu and (d) FMCN/Cu NLs as a function of h .

a previous experiment [44] shows that the fluctuation of lattice potential energy in HEAs produces more atomic traps and blocks, which gives rise to high activation energy and low atomic diffusion mobility. With abundant jumps in the process of diffusion and aggregation, most He atoms in HEAs can experience significant fluctuation in lattice potential energy and ultimately be trapped in the deep trap sites with low lattice potential energy [45]. It is suggested the characteristics of HEAs, e.g. the high entropy effect, the severe lattice distortion effect and the sluggish diffusion effect, confer their outstanding irradiation tolerance, as confirmed in other multicomponent alloy systems, such as TaWVCr [46] and TiZrHfVMo [47].

We elucidate the second finding that the bubble size d_{bub} of Cu layers and FMCC layers remains nearly constant about 1.4 nm and 0.8 nm, respectively, which is far smaller than that of FMCN/Cu NLs (~2.0 nm in Cu and ~1.4 nm in FMCN). A prior study [48] uncovered that one can tailor the composition of HEAs to reduce their phase stability, thereby obtaining dual-phase microstructure. The dual-phase microstructure not only causes remarkable interface hardening to increase the strength of materials, but also can strongly influence their irradiation tolerance. The FMCC/Cu NLs not only have numerous coherent interfaces, but also have abundant FCC-HCP phase interfaces which can be served as effective defects sinks. Prior studies [1,2] revealed that the interstitial atoms are preferred to be absorbed by interfaces. Therefore, in duplex FMCC layers, the FCC/HCP phase interfaces could further enhance the irradiation tolerance of FMCC/Cu NLs. In addition, previous studies [49] unveiled that in the austenitic stainless steels undergoing irradiation, Ni tends to enrich, while Cr and Mn deplete at GBs, and this irradiation-induced segregation behavior could be explained by the inverse Kirkendall mechanism (1 K) [5]. A recent study [50] showed that the type of elements have a great impact on the disorder of electronic system, in particular, those alloys containing

Cr can suppress the evolution of defects to some degree. In this regard, compared with FMCN with more pronounced heterogeneity in composition, FMCC could show better composition uniformity under irradiation. Specifically, Cr solute, in particular at high Cr concentrations, can strongly suppresses cavity swelling of ion irradiated alloys, such as Fe-Cr [51].

4.2. Size-dependent hardness and strengthening mechanisms

In general, the operation of deformation mechanisms, such as ordinary full dislocations, partial dislocations deformation twinning (or stacking faults, SFs) or GB-mediated mechanisms (GB sliding and/or grain rotation), are determined by the characteristic (or minimum) size of microstructure in a material. As the characteristic size is reduced from the micro-scale into the nanoscale, there is often a critical size D_c for the transition of plastic deformation mechanism from full to partial dislocations, which can be expressed as [52–55]:

$$D_c = \frac{2\beta\mu(mb_f - b_p)b_p}{\gamma} \quad (2)$$

where b reflects the character of the dislocation, m is the shear modulus, μ is a stress concentration factor, γ is the SFE, b_f and b_p is the magnitude of the Burgers vector of the full dislocations and partial dislocations. Taking the following parameters: $b = 1$, $m_{\text{Cu}} = 48.3$ GPa [56], $m_{\text{FMCC}} = 80$ GPa [57], $m_{\text{FMCN}} = 77$ GPa [58], $m = 2$, $b_f, \text{Cu} = 0.2556$ nm, $b_f, \text{FMCC} = 0.2531$ nm [57], $b_f, \text{FMCN} = 0.2539$ nm [57], $b_p, \text{Cu} = 0.1476$ nm, $b_p, \text{FMCC} = 0.1461$ nm [57], $b_p, \text{FMCN} = 0.1466$ nm [57], $g_{\text{Cu}} = 41$ mJ m⁻² [56], $g_{\text{FMCC}} = 31$ mJ m⁻² [57], $g_{\text{FMCN}} = 22$ mJ m⁻² [49], the estimated critical size D_c is about ~115, ~280 and ~352 nm for Cu, FMCC and FMCN layers, respectively. The calculated critical size D_c is much greater than the characteristic size of the corresponding constituent in as-deposited HEA/Cu NLs. It is suggested that partials emission from

boundaries is the dominant deformation mechanism. Moreover, the in-plane grain sizes of columnar HEA grains are very small, so that the large height-to-diameter ratio of grains (on the order of 50 nm/9 nm = 5.5) renders the activation of the GB-mediated mechanisms is quite difficult, in particular under the strong constraining effect caused by interfaces and GBs in NLs. Therefore, we in what follows discuss the strengthening mechanisms in both as-deposited and irradiated HEA/Cu NLs, based on the partial dislocation mechanism.

4.2.1. As-deposited HEA/Cu NLs

It is well-accepted that that strengthening behavior in conventional bimetal NLs can be divided by three distinctive regions in the full-length scale, i.e., the classic Hall-Petch model, the confined layer slip (CLS) model and interface barrier strength (IBS) model [59]. By reducing the length scale into the nano-regime, once the stress required for hairpin dislocation gliding in isolated layers is higher than the interfacial barrier for dislocation transmission, the deformation mechanism will change from CLS to IBS. Thus, we first determine the IBS of as-deposited HEA/Cu NLs by the following formula [56,60,61]:

$$\sigma_{\text{IBS}} = \sigma_K + \sigma_d + \sigma_{\text{ch}} = M\mu^* R \frac{\sin \varphi}{8\pi} + M\beta\mu^* \left(\zeta - \frac{b}{L} \right) + M \frac{\Delta\gamma}{b} \quad (3a)$$

where σ_K is the Koehler stress originating from modulus mismatch, σ_d related to misfit dislocations can be neglected due to the coherent interfaces in HEA/Cu NLs, and σ_{ch} is the chemical interaction term related to the difference in SFE of constituents. Thus, the IBS of HEA/Cu NLs can be given by:

$$\sigma_{\text{IBS}} \approx M\mu^* R \frac{\sin \varphi}{8\pi} + M \frac{\Delta\gamma}{b} \quad (3b)$$

where M is the Taylor factor, $\mu^* = 2 \frac{\mu_{\text{Cu}} \cdot \mu_{\text{HEA}}}{\mu_{\text{Cu}} + \mu_{\text{HEA}}}$ is the mean shear modulus, $R = \frac{\mu_{\text{HEA}} - \mu_{\text{Cu}}}{\mu_{\text{HEA}} + \mu_{\text{Cu}}}$, j is the angle between the slip plane and interface, $Dg = g_{\text{Cu}} - g_{\text{HEA}}$ is SFE difference and b is the magnitude of the Burgers vector (of a partial dislocation). Taking $M = 3$, and other parameters above, the estimated IBS is ~ 1.87 and ~ 1.92 GPa for FMCC/Cu and FMCN/Cu NLs, respectively, as indicated by the dash-dot lines in Fig. 11(a) and (c).

On the other hand, Misra et al. [62] proposed a refined CLS model considering the effect of dislocation core spreading along the interface, interface stress and resistance from interface dislocation arrays, as follows:

$$\sigma_{\text{CLS}} = \frac{M\mu b \sin \varphi}{8\pi h} \left(\frac{4-\nu}{1-\nu} \right) \ln \left(\frac{\alpha h}{b \sin \varphi} \right) - \frac{F}{h} + \frac{\mu f \varepsilon}{B(1-\nu)} \quad (4)$$

where a represents the core cut-off parameter in the range of 0–1, n is the Poisson's ratio, F is the characteristic interface stress of NLs, f is the volume fraction of constituent layers, ε is the in-plane plastic strain, B is a strain resolution factor of the order of 0.5 for the active slip system. Considering the essential characteristic of HEAs, the lattice friction s_0 cannot be ignored as a strengthening factor when dislocation glides in the HEA layer [63]. The intrinsic lattice stress s_0 can be predicted by a new solute strengthening theory based on the concept of misfit volume ΔV_n in HEAs [64], as below:

$$\tau_0 = A_\tau \chi^{-\frac{1}{3}} \mu \left[\frac{1+\nu}{1-\nu} \right]^{\frac{4}{3}} \left[\frac{\sum_n c_n \Delta V_n^2}{b^6} \right]^{\frac{2}{3}} \quad (5)$$

$$\Delta E_b = A_E \chi^{\frac{1}{3}} \mu b^3 \left[\frac{1+\nu}{1-\nu} \right]^{\frac{2}{3}} \left[\frac{\sum_n c_n \Delta V_n^2}{b^6} \right]^{\frac{1}{3}} \quad (6)$$

$$\sigma_0(T, \dot{\varepsilon}) = M\tau_0 \left[1 - \left(\frac{k_B T}{\Delta E_b} \ln \frac{\dot{\varepsilon}_0}{\dot{\varepsilon}} \right)^{\frac{2}{3}} \right] \quad (7)$$

where ΔV_n is the misfit volumes of each type element, c_n is the molar percent of component, k_B is the Boltzman constant $\sim 1.38 \times 10^{23} \text{ J K}^{-1}$, $T (\sim 298 \text{ K})$ is the temperature and $\dot{\varepsilon} (\sim 0.1 \text{ s}^{-1})$ is the strain rate, c is related to the edge dislocation line tension which is 0.125 for FCC alloys [65]. Taking the parameters: $A_\tau = 0.01785$, $A_E = 1.5618$ for FCC alloys [64] and $\zeta = 0.125$, $n_{\text{FMCC}} = 0.28$ [57], $n_{\text{FMCN}} = 0.28$ [57], $c_n = (0.5, 0.3, 0.1, 0.1)$, and $V_n = (12.09, 12.60, 11.12, 12.27, 10.94) \text{ \AA}^3$ [64] for Fe, Mn, Co, Cr and Ni, respectively, the lattice friction s_0 for FMCC HEAs is ~ 65.8 MPa and for FMCN HEAs is ~ 105.5 MPa. By contrast, the lattice friction s_0 for Cu is only ~ 25.5 MPa [66]. Also, given the columnar grains play a critical role in dislocation sliding, the layer thickness h is replaced by the effective size $h_{\text{eff}} = (h+2d)/3$ [67]. Therefore, the above refined CLS model can be further modified as follows:

$$\sigma_X = \sigma_0 + \frac{M\mu b_p \sin \varphi}{8\pi h_{\text{eff}}} \left(\frac{4-\nu}{1-\nu} \right) \ln \left(\frac{\alpha h_{\text{eff}}}{b_p \sin \varphi} \right) - \frac{F}{h} + \frac{\mu f \varepsilon}{B(1-\nu)} + P^T k_T \lambda_T^{-1/2} + (1-P^T) M \left(\frac{\gamma}{b_p} \right) \quad (8)$$

Due to the HEA/Cu NLs showing synergistic deformation, we approximately estimate the strength as follows [68]:

$$\sigma = \xi_{\text{Cu}} \cdot \sigma_{\text{Cu}} + \xi_{\text{HEA}} \cdot \sigma_{\text{HEA}} \quad (9)$$

where x_{Cu} and x_{HEA} are the deformed fraction contribution of the Cu and HEA layers, which could be taken as an equal value of 0.5 for the sake of simplicity. Taking $n_{\text{Cu}} = 0.343$, $a = 0.8$, $e_{\text{FMCC/Cu}} = 0.08\%$, $e_{\text{FMCN/Cu}} = 0.2\%$, $F = 2 \text{ J m}^{-2}$, $k_T = 3.4 \text{ GPa nm}^{1/2}$ [69], $P_{\text{FMCC/Cu}}^T = 61\%$, $P_{\text{FMCN/Cu}}^T = 72\%$, $\lambda_{\text{FMCC/Cu}}^T = 5.2 \text{ nm}$, $\lambda_{\text{FMCN/Cu}}^T = 5.4 \text{ nm}$. Substituting Eq. (8) to Eq. (9), the calculated hardness agrees well with the experimental results in the Regime-I, as shown in Fig. 11(a, c) with the green and blue solid lines for FMCC/Cu and FMCN/Cu NLs, respectively.

However, in the Regime-II, the deformation mechanism above does not work in the present HEA/Cu NLs, and the modified CLS model, i.e., Eq. (8) underestimates their strength in this large length scale. In this regime, dislocation nucleation process, which needs relatively higher applied stresses, becomes the dominant mechanism to govern the strength of HEA/Cu NLs. Given the HEA layers have much smaller grain sizes, so that dislocations in HEA layers are more likely to be emitted from GBs and propagate during deformation. Therefore, the strength of HEA/Cu NLs can be considered as the critical stress needed to emit partial dislocations in HEA layers, which can be given by [52–54]:

$$\sigma_{\text{Partial}} = \frac{1}{m \cdot s} \left(\frac{2\beta\mu b_p}{d} + \frac{\gamma}{b_p} \right) \quad (10)$$

where s is the Schmid factor of the corresponding slip system of ~ 0.27 – 0.41 [53]. The grain size d of HEA layers in the Regime-II is ~ 9.8 – 12.1 nm and ~ 10.3 – 10.9 nm for FMCC/Cu and FMCN/Cu NLs, respectively. Taking $s = 0.41$ and other parameters are same as above, the predicted hardness ($= 2.7 \times s_{\text{partial}}$) ranges are depicted as the light pink and light blue regions for FMCC/Cu and FMCN/Cu NLs in Fig. 11(a) and (c), respectively. It is found that the measured hardness of HEA/Cu NLs falls well in the range of the predicted hardness of HEA layers. In addition, the corresponding hardness of critical partial emission stress in Cu layer is only ~ 1.38 GPa, which is much smaller than the measured hardness of HEA/Cu NLs. These results indicate that it is the hard phase HEA layers rather than soft Cu layers that govern the hardness of HEA/Cu NLs.

4.2.2. Irradiated $Fe_{50}Mn_{30}Co_{10}Cr_{10}/Cu$ NLs

Prior studies often assume that the He bubbles are weaker obstacles than voids and serve as shearable obstacles for dislocation motion [30,35]. However, the stability and pinning effect of He bubbles on the gliding dislocations are closely dependent on the bubble pressure, which is closely related to the bubble sizes. Therefore, the estimation of bubble pressure is very important to quantify the irradiation hardening behavior.

As for the equilibrium He bubble, the bubble pressure is related to its size and the surface energy, which can be given by the Young-Laplace equation [26,70]:

$$P_{\text{bubble}} = \frac{2\gamma_s}{R} \quad (11)$$

where γ_s is the surface energy and R is the bubble radius. However, previous studies [69] revealed that He bubbles, activated to impose a local strain field with high internal pressure, are expected to drastically influence the adjacent defects production and microstructure evolution in irradiated materials, even promote nucleation and emission of partials, so that the Young-Laplace equation cannot accurately capture the state of over-pressurized He bubbles. As for the bubbles with extremely high pressure, the pressure of the bubbles can be determined by the upper bound limit of materials property, which can be given by [70]:

$$P \leq 0.2\mu \quad (12)$$

where μ is the shear modulus. Pressurized He bubbles could lead to lattice expansion based on the point source dilatation mechanism. When the bubble radius and the spacing between He bubbles are smaller, the representative displacement field of a bubble of expansion has greater influence [26]. A recent study [71] showed that in NT Ag films, compared with the large faceted bubbles with high dpa, the spherical bubbles under the condition of low dpa carry much higher He pressure and He-to-vacancy ratio. With loop punching and bubble migration and coalescence, various bubble growth and coarsening mechanisms may cause the release of bubble pressure. Based on the dense bubble distribution and small spherical bubble shape in FMCC/Cu NLs, the calculated upper limit of bubble pressure in Cu of FMCC/Cu NLs is 9.7 GPa and the bubble pressure in FMCC is 16 GPa. According to calculated data, it is obvious that the He bubbles in the irradiated FMCC/Cu NLs are over-pressurized and can be considered as strong obstacles comparable to small voids.

As revealed previously, He bubbles as the main irradiation defects in FMCC/Cu NLs have strong effects on the microstructural evolution on the one hand and result in the notable irradiation hardening on the other hand [1,2]. Specifically, these He bubbles at layer interfaces will significantly interfere with the transmission of partials, because the over-pressurized He bubbles are usually strong obstacles [31,72]. In other words, the interface decorated by He bubbles may become strong enough and only allow the transmission of full rather than partial dislocations [31]. Actually, for the present irradiated FMCC/Cu NLs, the measured hardness is lower than the theoretical IBS (see Fig. 11(a)), thus the dislocation motion is still confined inside the isolated layers. Given the much smaller sizes and higher densities of He bubbles in the irradiated FMCC/Cu NLs, we simply assume that the gliding dislocations are pinned by these impenetrable obstacles (i.e., He bubbles) with spacing l_{bub} [25,72]. During indentation tests, these weak pinning points can be overcome at the applied shear stresses less than that needed to bend a dislocation to the semicircle, and the hardening due to dislocation pinning at point obstacles can be written as [26,73]:

$$\Delta\tau = \frac{\mu b_p}{2\pi l_{\text{bub}}} \left[\ln \left(d_{\text{bub}}^{-1} + l_{\text{bub}}^{-1} \right)^{-1} + \omega \right] \quad (13)$$

where d_{bub} is the diameter of He bubbles, l_{bub} is the bubble spacing, μ is the shear modulus, b_p is the magnitude of the Burgers

vector of a partial and ω is an empirical constant ~ 0.85 (for impenetrable obstacles) [26]. Because the constituents of FMCC/Cu NLs show synergistic deformation behavior, we approximately estimate the irradiation hardening as follows:

$$\Delta H_{\text{Bubble}} = \xi_{\text{Cu}} \Delta H_{\text{Bubble}}^{\text{Cu}} + \xi_{\text{HEA}} \Delta H_{\text{Bubble}}^{\text{HEA}} \quad (14)$$

Taking $b_{p,\text{Cu}} = 0.1476$ nm, $b_{p,\text{FMCC}} = 0.1461$ nm, $\mu_{\text{Cu}} = 48$ GPa, $\mu_{\text{FMCC}} = 80$ GPa and $\xi_{\text{Cu}} = \xi_{\text{FMCC}} = 0.5$, the increase in hardness ($\Delta H = 2.7 \times 3.06 \times \Delta\tau$) from He bubbles can be calculated. The increased hardness of irradiated FMCC/Cu NLs with h in the range of $100 \text{ nm} \geq h > 5 \text{ nm}$ can be well fit by Eqs. (13) and (14), see Fig. 11(b).

Although the IBS of FMCC/Cu NLs is larger than the stress required for CLS of partials, the motion of partial dislocations cannot be confined within isolated layers when there are more than two partials on a slip plane. This is because that the leading partial dislocation can transmit across the coherent interface, when the exerting stress on the leading dislocation overcomes the interface barrier according to the dislocation pile-up theory. Indeed, Zhao et al. [74] uncovered that at extremely small h , both Cu or Ni and HEA constituents co-deform and almost contribute to the plastic strain equally. In this scenario ($\xi_{\text{Cu}} = \xi_{\text{FMCC}} = 0.5$), however, this model far underestimates the irradiation hardening in FMCC/Cu NLs with $h = 5 \text{ nm}$, because that it is difficult to observe He bubbles in FMCC layers with $\Delta H_{\text{Bubble}}^{\text{HEA}} = 0$, as depicted by the specific spot in Fig. 11(b). Previous studies [70] pointed out that the calculated He concentration stored in He bubbles is much lower than the value predicted by SRIM simulations, implying that most He atoms exist in the form of He-vacancy clusters. In this regard, a possible reason for the discrepancy between the experiment and the theoretical calculation is the irradiation hardening raised by He-vacancy clusters that are below the resolution limit of TEM. Also, it appears that this model overestimates the hardness of the irradiated FMCC/Cu NLs with $h > 100 \text{ nm}$. This is because that there are numerous bubble chains in these large h samples, which facilitate plastic deformation and result in softening of materials. In other words, the bubble chains make the measured hardness lower than the predicted one at $h > 100 \text{ nm}$.

4.2.3. Irradiated $Fe_{50}Mn_{30}Co_{10}Ni_{10}/Cu$ NLs

Previous work [70] has proved that the pressure of larger faceted shape bubbles is much lower than that of small-sized bubbles. Given the larger faceted shape and a lower density of He bubbles in irradiated FMCN/Cu NLs, we simply assume that these He bubbles serve as shearable obstacles for dislocation motion [34,36–38] and the force obstacles exert on the dislocations is confined to a small segment of dislocations over a long bowed-out length. Under this condition, the total force exerted on the dislocation line can be considered as the sum of individual force produced by each obstacle. The increase of stress (or irradiation hardening) due to He bubbles can be obtained by the equilibrium between the line force and resistance of all obstacles over the length. To carry plasticity, dislocations are forced to bow out and then cut these shearable bubbles, as identified in He irradiated Cu [30]. In this case, the irradiation hardening (ΔH) caused by dislocation pinning by He bubbles can be given by [2]:

$$\Delta H_{\text{bubble}} = 2.7M\tau_i \left(1 - \frac{l_{\text{bub}}^{\text{layer}}}{\sqrt{2}h} \right) \quad (15)$$

Unlike the case of FMCC/Cu NLs, the irradiation hardening behavior in the irradiated $Fe_{50}Mn_{30}Co_{10}Ni_{10}/Cu$ NLs can be categorized into two regimes by a critical layer thickness h ($\sim 50 \text{ nm}$), as discussed below.

(i) When $h \leq 50 \text{ nm}$, the irradiation hardening of FMCN/Cu NLs increases with increasing h , similar to conventional bimetal NLs.

Since the IBS is in between the strength of as-deposited and irradiated FMCN/Cu NLs, the propagation of single dislocations in the CLS regime ($\sim 50 \text{ nm} \geq h > \sim 5 \text{ nm}$) would be confined inside a layer under a low-stress level, and then these single dislocations could cut across interfaces containing a distribution of nanosized He bubbles in the interface plane under a high-stress level. The He bubbles in NLs as weak shearable obstacles to gliding dislocations can cause irradiation hardening. Taking $\xi_{\text{Cu}} = \xi_{\text{FMCN}} = 0.5$ and other statistical data into Eqs. (14) and (15), the estimated hardening agrees well with the experimental data, as shown in Fig. 11(d). For the $h = 5 \text{ nm}$ FMCN/Cu NLs, He bubbles cannot be detected in FMCN layers, similar to the case of FMCC/Cu NLs. The calculated result of irradiated FMCN/Cu NLs with $h = 5 \text{ nm}$ also far underestimates the experimental data, owing to the same reason mentioned above, i.e., He-vacancy cluster hardening in FMCC/Cu NLs.

(ii) When $h > 50 \text{ nm}$, the smaller bubbles in the grain interior may serve to pin the glide dislocations traversing the grains, resulting in a hardening effect, while the continuous bubble chain formed at GBs in a layer (see Fig. 5(d)) may facilitate dislocation emission and GB sliding, resulting in softening during deformation [37]. Therefore, it is reasonable that the irradiation hardening decreases with increasing h at this large h -regime.

4.3. Size-dependent strain rate sensitivity of HEA/Cu NLs

In general, the SRS m of conventional twin-free bimetal NLs is positive and strongly h -dependent, such as Cu/Cr [75], Cu/Mo [28] and Cu/Zr [34]. In other words, these bimetal NLs manifest monotonically increased SRS m with reducing h or increasing the density of interfaces. However, in sharp contrast to these bimetal NLs, the present two kinds of as-deposited HEA/Cu NLs manifest unusually inverse h -dependent SRS m , namely smaller h leads to lower SRS m . Moreover, at a given h , compared with the as-deposited NLs, the FMCC/Cu NLs exhibit increased SRS m , while the FMCN/Cu ones show reduced SRS m after He-ion irradiation. The underlying reasons for these unique behaviors can be rationalized in terms of two competing aspects, including positive factors that increase SRS m and negative factors that decrease SRS m .

In fact, apart from the interface/boundary that can enhance positive SRS m of materials via dislocation-interface/boundary interactions, currently, it is accepted that the nanotwins can increase the positive SRS m of materials, and thinner nanotwins and/or higher fractions of nanotwins can notably increase SRS m , as uncovered in pure Cu [41] and Ni [76] metals and FeCoCrNi-based HEAs [77]. Nevertheless, the phase transformation [78] and dynamic strain aging [79] often induce negative SRS m of metallic materials. For example, Wang et al. [78] observed that the phase-transformation-induced negative SRS m only occurs in β -Ta (but not in α -Ta) during nanoindentation deformation. Li et al. [79] uncovered that adding Mg atoms into the Cu matrix would reduce the SRS m of Cu, due to the dynamic strain aging effect via solute atom-dislocation interactions. Based on these factors, we separately discuss the inverse- h dependent SRS m in FMCC/Cu and FMCN/Cu NLs below.

For the as-deposited FMCC/Cu NLs, the monotonically increased density of interface/boundary (or reduced h) would induce the increased positive SRS m . At the same time, although the present FMCC/Cu NLs have the minimum fraction of twins at $h = 25 \text{ nm}$, the twin thickness λ reduces from 9.5 to 5.3 nm with reducing h from 150 to 5 nm, rendering the SRS of FMCC/Cu NLs increase. On the other hand, at large $h > 10 \text{ nm}$, the FMCC layers exhibit dual-phase structure, while at small $h \leq 10 \text{ nm}$ the FMCC layers become the single phase. However, phase transformation is more preferred to occur at small h , due to size constraining effects, leading to negative SRS m . Therefore, these two competing effects on rate sensitivity induce the inverse h -dependent SRS m , which de-

creases with reducing h . After He-ion irradiation, the dislocations interact with impenetrable bubbles in a way similar to the scenario of dislocation-solute atoms interactions, which can cause the dynamic strain aging effect. Moreover, because these highly pressurized He bubbles, serving as strong obstacles for dislocation motion, promote SF-mediated deformation in FMCC layers [80], these He bubbles cannot suppress the occurrence of phase transformation via the formation of SFs [80]. These in turn render that compared with the as-deposited samples, the SRS m sharply drops at a given h in the irradiated FMCC/Cu NLs, even becomes negative.

Similar to the case of as-deposited FMCC/Cu NLs, the reduced negative SRS m in the as-deposited FMCN/Cu NLs can also be mainly attributed to the above two competing aspects. However, after He-implantation, these shearable He bubbles as predominant defect sources, do not hinder the SF-mediated phase transformation behavior [80]. This still contributes to the negative SRS m . However, due to the shearable nature of He bubbles, the significant dislocation-bubble interactions that contribute to the positive SRS can notably increase m . In this regard, compared with the as-deposited FMCC/Cu NLs, the irradiated samples manifest enhanced SRS m .

5. Conclusions

In this work, we investigated the HEA/Cu NLs ($\text{HEA} = \text{Fe}_{50}\text{Mn}_{30}\text{Co}_{10}\text{Cr}_{10}$, $\text{Fe}_{50}\text{Mn}_{30}\text{Co}_{10}\text{Ni}_{10}$) before and after He-ion irradiation, in terms of microstructural evolution and mechanical properties, including hardness and strain rate sensitivity (SRS). The main findings provide new insights into designing the nanolaminates containing HEAs with the desirable ability of irradiation resistance and mechanical properties, which are summarized as follows:

- (1) Compared with FMCN/Cu NLs, the FMCC/Cu NLs, in which the duplex HEA layers exist FCC and HCP phases, exhibit better irradiation resistance with smaller h by curtailing the bubble size, thus alleviating irradiation swelling.
- (2) The hardness of transformable HEA/Cu NLs manifests two size-dependent regimes, i.e., at small h , they display the trend of “smaller is stronger” (similar to conventional bimetal NLs), while at large h , they display the size-independent hardness plateau. The $\text{Fe}_{50}\text{Mn}_{30}\text{Co}_{10}\text{Cr}_{10}/\text{Cu}$ NLs exhibit the monotonically increased irradiation hardening with decreasing h . Because of the pressurized He bubbles, dislocations are pinned by these impenetrable obstacles causing the unusual trend. In the $\text{Fe}_{50}\text{Mn}_{30}\text{Co}_{10}\text{Ni}_{10}/\text{Cu}$ NLs, the bubble chains facilitate GB sliding, resulting in softening, while the dislocations are hindered by penetrable He bubbles, causing strengthening. Owing to these two competing effects, the irradiation hardening exhibits the maximum at $h = 50 \text{ nm}$.
- (3) Contrary to conventional bimetal NLs, the present HEA/Cu NLs manifest inverse layer thickness h -dependent SRS before and after irradiation. However, compared with the as-deposited HEA/Cu NLs, the irradiated $\text{Fe}_{50}\text{Mn}_{30}\text{Co}_{10}\text{Cr}_{10}/\text{Cu}$ NLs exhibit reduced SRS m , while the irradiated $\text{Fe}_{50}\text{Mn}_{30}\text{Co}_{10}\text{Ni}_{10}/\text{Cu}$ NLs exhibit enhanced SRS m , which is dependent on the characters of He bubbles.

Declaration of Competing Interest

The authors declare that they have no known competing financial interests or personal relationships that could have appeared to influence the work reported in this paper.

Acknowledgments

This work was financially supported by the National Natural Science Foundation of China (Nos. U2067219, 51722104, 51790482, 51761135031 and 92163201), the National Key Research and Development Program of China (No. 2017YFA0700701), the 111 Project 2.0 of China (No. BP2018008), and the Fundamental Research Funds for the Central Universities (No. xtr022019004). We would thank S.W. Guo, Y.H. Li and J. Li for their kind help with the microstructural characterization of materials.

Supplementary materials

Supplementary material associated with this article can be found, in the online version, at doi:[10.1016/j.jmst.2021.10.036](https://doi.org/10.1016/j.jmst.2021.10.036).

References

- [1] I.J. Beyerlein, M.J. Demkowicz, A. Misra, B.P. Uberuaga, *Prog. Mater. Sci.* 74 (2015) 125–210.
- [2] X. Zhang, K. Hattar, Y. Chen, L. Shao, J. Li, C. Sun, K. Yu, N. Li, M.L. Taheri, H. Wang, J. Wang, M. Nastasi, *Prog. Mater. Sci.* 96 (2018) 217–321.
- [3] S.J. Zinkle, G.S. Was, *Acta Mater.* 61 (2013) 735–758.
- [4] T.N. Yang, C. Lu, K. Jin, M.L. Crespillo, Y. Zhang, H. Bei, L. Wang, *J. Nucl. Mater.* 488 (2017) 328–337.
- [5] C. Lu, T. Yang, K. Jin, N. Gao, P. Xiu, Y. Zhang, F. Gao, H. Bei, W.J. Weber, K. Sun, Y. Dong, L. Wang, *Acta Mater.* 127 (2017) 98–107.
- [6] C. Lu, L. Niu, N. Chen, K. Jin, T. Yang, P. Xiu, Y. Zhang, F. Gao, H. Bei, S. Shi, M.R. He, I.M. Robertson, W.J. Weber, L. Wang, *Nat. Commun.* 7 (2016) 13564.
- [7] Y. Zhang, G.M. Stocks, K. Jin, C. Lu, H. Bei, B.C. Sales, L. Wang, L.K. Béland, R.E. Stoller, G.D. Samolyuk, M. Caro, A. Caro, W.J. Weber, *Nat. Commun.* 6 (2015) 8736.
- [8] G. Pu, L. Lin, R. Ang, K. Zhang, B. Liu, B. Liu, T. Peng, S. Liu, Q. Li, *Appl. Surf. Sci.* 516 (2020) 146129.
- [9] W. Chen, X. Ding, Y. Feng, X. Liu, K. Liu, Z.P. Lu, D. Li, Y. Li, C.T. Liu, X.-Q. Chen, *J. Mater. Sci. Technol.* 34 (2018) 355–364.
- [10] E.P. George, D. Raabe, R.O. Ritchie, *Nat. Rev. Mater.* 4 (2019) 515–534.
- [11] Y. Zou, H. Ma, R. Spolenak, *Nat. Commun.* 6 (2015) 7748.
- [12] Z. An, S. Mao, Y. Liu, H. Zhou, Y. Zhai, Z. Tian, C. Liu, Z. Zhang, X. Han, *J. Mater. Sci. Technol.* 92 (2021) 195–207.
- [13] C.C. Juan, M.H. Tsai, C.W. Tsai, C.M. Lin, W.R. Wang, C.C. Yang, S.K. Chen, S.J. Lin, J.W. Yeh, *Intermetallics* 62 (2015) 76–83.
- [14] J. Li, H. Chen, Q. Fang, C. Jiang, Y. Liu, P.K. Liaw, *Inter. J. Plast.* 133 (2020) 102819.
- [15] B. Gludovatz, A. Hohenwarter, D. Catoor, E.H. Chang, E.P. George, R.O. Ritchie, *Science* 345 (2014) 1153–1158.
- [16] H. Li, H. Jing, L. Xu, Y. Han, L. Zhao, Z. Tang, B. Xiao, Y. Zhang, *Inter. J. Plast.* 118 (2019) 105–129.
- [17] Z. Wang, C. Wang, Y.-L. Zhao, Y.-C. Hsu, C.-L. Li, J.-J. Kai, C.-T. Liu, C.-H. HSueh, *Int. J. Plast.* 131 (2020) 102726.
- [18] B. Cantor, I.T.H. Chang, P. Knight, A.J.B. Vincent, *Mater. Sci. Eng. A* 375–377 (2004) 213–218.
- [19] J.W. Yeh, S.K. Chen, S.J. Lin, J.Y. Gan, T.S. Chin, T.T. Shun, C.H. Tsau, S.Y. Chang, *Adv. Eng. Mater.* 6 (5) (2004) 299–303.
- [20] Y. Zhang, T.T. Zu, Z. Tang, M.C. Gao, K.A. Dahmen, P.K. Liaw, Z.P. Lu, *Prog. Mater. Sci.* 61 (2014) 1–93.
- [21] Z. Li, K.G. Pradeep, Y. Deng, D. Raabe, C.C. Tasan, *Nature* 534 (2016) 227–230.
- [22] Q. Fang, Y. Chen, J. Li, C. Jiang, B. Liu, Y. Liu, P.K. Liaw, *Int. J. Plast.* 114 (2019) 161–173.
- [23] M. Bahramyan, R.T. Mousavian, D. Brabazon, *Int. J. Plast.* 127 (2020) 102649.
- [24] S.M. Vakili, A. Zarei-Hanzaki, A.S. Anoushe, H.R. Abedi, M.H. Mohammad-Ebrahimi, M. Jaskari, S.S. Sohn, D. Ponge, L.P. Karjalainen, *Acta Mater.* 185 (2020) 474–492.
- [25] S.Q. Xia, W. Zheng, T.F. Yang, Y. Zhang, *J. Iron Steel Res. Int.* 22 (2015) 879–884.
- [26] N. Li, M. Nastasi, A. Misra, *Int. J. Plast.* 32–33 (2012) 1–16.
- [27] B.L. Hansen, J.S. Carpenter, S.D. Sintay, C.A. Bronkhorst, R.J. McCabe, J.R. Mayeur, H.M. Mourad, I.J. Beyerlein, N.A. Mara, S.R. Chen, G.T. Gray, *Int. J. Plast.* 49 (2013) 71–84.
- [28] J.Y. Zhang, F.L. Zeng, K. Wu, Y.Q. Wang, X.Q. Liang, G. Liu, G.J. Zhang, J. Sun, *Mater. Sci. Eng. A* 673 (2016) 530–540.
- [29] E.G. Fu, A. Misra, H. Wang, L. Shao, X. Zhang, *J. Nucl. Mater.* 407 (2010) 178–188.
- [30] Q.M. Wei, N. Li, N. Mara, M. Nastasi, A. Misra, *Acta Mater.* 59 (2011) 6331–6340.
- [31] Y. Chen, Y. Liu, E.G. Fu, C. Sun, K.Y. Yu, M. Song, J. Li, Y.Q. Wang, H. Wang, X. Zhang, *Acta Mater.* 84 (2015) 393–404.
- [32] M. Wang, I.J. Beyerlein, J. Zhang, W.-Z. Han, *Acta Mater.* 160 (2018) 211–223.
- [33] K.Y. Yu, Y. Liu, E.G. Fu, Y.Q. Wang, M.T. Myers, H. Wang, L. Shao, X. Zhang, *J. Nucl. Mater.* 440 (2013) 310–318.
- [34] X.Q. Liang, Y.Q. Wang, J.T. Zhao, S.H. Wu, K. Wu, G. Liu, J. Sun, *Surf. Coat. Technol.* 366 (2019) 255–265.
- [35] N. Li, E.G. Fu, H. Wang, J.J. Carter, L. Shao, S.A. Maloy, A. Misra, X. Zhang, *J. Nucl. Mater.* 389 (2009) 233–238.
- [36] S.H. Wu, P.M. Cheng, K. Wu, Z.Q. Hou, Y.Q. Wang, X.Q. Liang, J. Li, J. Kuang, J.Y. Zhang, G. Liu, J. Sun, *Int. J. Plast.* 111 (2018) 36–52.
- [37] X.Q. Liang, Y.Q. Wang, J.T. Zhao, S.H. Wu, X.B. Feng, K. Wu, J.Y. Zhang, G. Liu, J. Sun, *Mater. Sci. Eng. A* 764 (2019) 138259.
- [38] J.Y. Zhang, Y.Q. Wang, X.Q. Liang, F.L. Zeng, G. Liu, J. Sun, *Acta Mater.* 92 (2015) 140–151.
- [39] D. Pan, A. Inoue, T. Sakurai, M.W. Chen, *Proc. Natl. Acad. Sci.* 105 (2008) 14769.
- [40] R.E. Stoller, M.B. Toloczko, G.S. Was, A.G. Certain, S. Dwarkadas, F.A. Garner, *Nucl. Instrum. Methods B* 310 (2013) 75–80.
- [41] J. Chen, L. Lu, K. Lu, *Scr. Mater.* 54 (2006) 1913–1918.
- [42] M.J. Demkowicz, R.G. Hoagland, J.P. Hirth, *Phys. Rev. Lett.* 100 (2008) 136102.
- [43] A. Kashinath, A. Misra, M.J. Demkowicz, *Phys. Rev. Lett.* 110 (2013) 086101.
- [44] D. Chen, Y. Tong, H. Li, J. Wang, Y.L. Zhao, A. Hu, J.J. Kai, *J. Nucl. Mater.* 501 (2018) 208–216.
- [45] S. Zhao, Y. Zhang, W.J. Weber, *Enc. Mater. Met. Alloys* 2 (2022) 533–547.
- [46] S. Zhao, *J. Mater. Sci. Technol.* 44 (2020) 133–139.
- [47] Y. Lu, H. Huang, X. Gao, C. Ren, J. Gao, H. Zhang, S. Zheng, Q. Jin, Y. Zhao, C. Lu, T. Wang, T. Li, *J. Mater. Sci. Technol.* 35 (2019) 369–373.
- [48] J.W. Brooks, M.H. Loretto, R.E. Smallman, *Acta Metall.* 27 (1979) 1839–1847.
- [49] G.S. Was, J.P. Wharry, B. Frisbie, B.D. Wirth, D. Morgan, J.D. Tucker, T.R. Allen, *J. Nucl. Mater.* 411 (2011) 41–50.
- [50] K. Jin, C. Lu, L.M. Wang, J. Qu, W.J. Weber, Y. Zhang, H. Bei, *Scr. Mater.* 119 (2016) 65–70.
- [51] Y.R. Lin, A. Bhattacharya, D. Chen, J.J. Kai, J. Henry, S.J. Zinkle, *Acta Mater.* 207 (2021) 116660.
- [52] M.W. Chen, E. Ma, K.J. Hemker, H.W. Sheng, Y.M. Wang, X.M. Cheng, *Science* 300 (2003) 1275.
- [53] P.A. Gruber, J. Böhm, F. Onuseit, A. Wanner, R. Spolenak, E. Arzt, *Acta Mater.* 56 (2008) 2318–2335.
- [54] J.Y. Zhang, G. Liu, R.H. Wang, J. Li, J. Sun, E. Ma, *Phys. Rev. B* 81 (2010) 172104.
- [55] Z.X. Wu, Y.W. Zhang, D.J. Srolovitz, *Acta Mater.* 57 (2009) 4508–4518.
- [56] Y. Liu, Y. Chen, K.Y. Yu, H. Wang, J. Chen, X. Zhang, *Int. J. Plast.* 49 (2013) 152–163.
- [57] S.F. Liu, Y. Wu, H.T. Wang, J.Y. He, J.B. Liu, C.X. Chen, X.J. Liu, H. Wang, Z.P. Lu, *Intermetallics* 93 (2018) 269–273.
- [58] Z. Wu, H. Bei, G.M. Pharr, E.P. George, *Acta Mater.* 81 (2014) 428–441.
- [59] J.Y. Zhang, K. Wu, L.Y. Zhang, Y.Q. Wang, G. Liu, J. Sun, *Int. J. Plast.* 96 (2017) 120–134.
- [60] J.S. Koehler, *Phys. Rev. B* 2 (1970) 547–551.
- [61] S.I. Rao, P.M. Hazzledine, *Philos. Mag. A* 80 (2000) 2011–2040.
- [62] A. Misra, J.P. Hirth, R.G. Hoagland, *Acta Mater.* 53 (2005) 4817–4824.
- [63] X.B. Feng, J.Y. Zhang, Y.Q. Wang, Z.Q. Hou, K. Wu, G. Liu, J. Sun, *Int. J. Plast.* 95 (2017) 264–277.
- [64] C. Varvenne, A. Luque, W.A. Curtin, *Acta Mater.* 118 (2016) 164–176.
- [65] B. Yin, F. Maresca, W.A. Curtin, *Acta Mater.* 188 (2020) 486–491.
- [66] X.G. Li, L.F. Cao, J.Y. Zhang, J. Li, J.T. Zhao, X.B. Feng, Y.Q. Wang, K. Wu, P. Zhang, G. Liu, J. Sun, *Acta Mater.* 151 (2018) 87–99.
- [67] M.S. Colla, B. Wang, H. Idriessi, D. Schryvers, J.P. Raskin, T. Pardo, *Acta Mater.* 60 (2012) 1795–1806.
- [68] Z. Fan, Y. Liu, S. Xue, R.M. Rahimi, D.F. Bahr, H. Wang, X. Zhang, *Appl. Phys. Lett.* 110 (2017) 611.
- [69] X.H. Chen, L. Lu, K. Lu, *Scr. Mater.* 64 (2011) 311–314.
- [70] Z. Shang, J. Ding, C. Fan, D. Chen, J. Li, Y. Zhang, Y. Wang, H. Wang, X. Zhang, *Acta Mater.* 196 (2020) 175–190.
- [71] T. Niu, J. Li, Y. Zhang, J. Cho, J. Ding, R. Su, S. Xue, C. Fan, Z. Shang, D. Chen, Y. Wang, H. Wang, X. Zhang, *J. Nucl. Mater.* 540 (2020) 152392.
- [72] S.H. Li, J.T. Li, W. Han, *Materials (Basel)* 12 (2019) 1036.
- [73] B.A. Szajewski, J.C. Crone, J. Knop, *Materials* 11 (2020) 100671.
- [74] Y.F. Zhao, X.B. Feng, J.Y. Zhang, Y. Lu, S.H. Wu, Y.Q. Wang, K. Wu, G. Liu, J. Sun, *Nanoscale* 12 (2020) 14135–14149.
- [75] J.J. Niu, J.Y. Zhang, G. Liu, P. Zhang, S.Y. Lei, G.J. Zhang, J. Sun, *Acta Mater.* 60 (2012) 3677–3689.
- [76] G. Sharma, P. Mukherjee, A. Chatterjee, N. Gayathri, A. Sarkar, J.K. Chakravarthy, *Acta Mater.* 61 (2013) 3257–3266.
- [77] X.B. Feng, W. Fu, J.Y. Zhang, J.T. Zhao, J. Li, K. Wu, G. Liu, J. Sun, *Scr. Mater.* 139 (2017) 71–76.
- [78] Y.M. Wang, A.M. Hodge, P.M. Bythrow, T.W. Barbee, A.V. Hamza, *Appl. Phys. Lett.* 89 (2006) 081903.
- [79] G.Y. Li, L.F. Cao, J.Y. Zhang, X.G. Li, Y.Q. Wang, K. Wu, G. Liu, J. Sun, *J. Mater. Sci. Technol.* 57 (2020) 101–112.
- [80] W.T. Lin, D. Chen, C.Q. Dang, P.J. Yu, G. Wang, J.H. Lin, F.L. Meng, T. Yang, Y.L. Zhao, S.F. Liu, J.P. Du, G.M. Yeli, C.T. Liu, Y. Lu, S. Ogata, J.J. Kai, *Acta Mater.* 210 (2021) 116843.